

Protostars and Outflows in the NGC 7538 - IRS 9 Cloud Core

Göran Sandell¹, W. M. Goss², and Melvyn Wright³

gsandell@mail.arc.nasa.gov

ABSTRACT

New high resolution observations of HCO^+ $J=1 \rightarrow 0$, H^{13}CN $J=1 \rightarrow 0$, SO $2_2 \rightarrow 1_1$, and continuum with BIMA at 3.4 mm show that the NGC 7538 - IRS 9 cloud core is a site of active ongoing star formation. Our observations reveal at least three young bipolar molecular outflows, all $\sim 10,000 - 20,000$ years old. IRS 9 drives a bipolar, extreme high velocity outflow observed nearly pole on. South of IRS 9 we find a cold, protostellar condensation with a size of $\sim 14'' \times 6''$ with a mass $> 250 M_\odot$. This is the center of one of the outflows and shows deep, red-shifted self absorption in HCO^+ , suggesting that there is a protostar embedded in the core, still in a phase of active accretion. This source is not detected in the far infrared, suggesting that the luminosity $< 10^4 L_\odot$; yet the mass of the outflow is $\sim 60 M_\odot$. The red-shifted HCO^+ self-absorption profiles observed toward the southern protostar and IRS 9 predict accretion rates of a few times 10^{-4} to $10^{-3} M_\odot \text{ yr}^{-1}$. Deep VLA continuum observations at 3.6 cm show that IRS 9 coincides with a faint thermal VLA source, but no other young star in the IRS 9 region has any detectable free-free emission at a level of $\sim 60 \mu\text{Jy}$ at 3.6 cm. The HCO^+ abundance is significantly enhanced in the hot IRS 9 outflow. A direct comparison of mass estimates from HCO^+ and CO for the well-characterized red-shifted IRS 9 outflow predicts an HCO^+ enhancement of more than a factor of 30, or $[\text{HCO}^+/\text{H}_2] \geq 6 \cdot 10^{-8}$.

Subject headings: ISM: clouds – ISM: molecules – radio lines – ISM:masers – ISM: individual – NGC 7538 - IRS 9 (stars:) circumstellar matter – stars: formation – stars: pre-main sequence

¹SOFIA-USRA, NASA Ames Research Center, MS N211-3, Moffett Field, CA 94035, U.S.A.

²National Radio Astronomy Observatory, P.O. Box O, Socorro, NM 87801, U.S.A.

³Radio Astronomy Laboratory, University of California, Berkeley 601 Campbell Hall, Berkeley, CA 94720, U.S.A.

1. Introduction

Massive stars form in associations or clusters together with hundreds of intermediate and low-mass stars (Hillenbrand 1977). Although it is still not conclusively proven that high-mass stars form the same way as low-mass stars, i.e. with accretion disks supporting accretion and driving outflows, recent theoretical models show that high accretion rates and the pressure from surrounding massive cloud cores are sufficient to overcome radiation pressure from a newly formed high-mass star, therefore allowing the stellar mass to increase far above the theoretical limit of $8 M_{\odot}$ (Maeder & Behrend 2002; McKee & Tan 2002). Recent surveys of high-mass star formation regions (Henning et al. 2000; Zhang et al. 2001) show that molecular outflows are common in high-mass young stars. Accretion disks, however, are far more difficult to detect, because high-mass protostars are more distant and deeply embedded than low-mass stars, and since they form in clusters or small groups it is difficult to isolate and image disks around high-mass protostars, because of confusion and poor spatial resolution. Yet, there are several results that show rather convincingly that high-mass protostars are surrounded by rotating accretion disks (Cesaroni et al. 1997; Zhang, Hunter, & Sridharan 1998; Sandell, Wright & Forster 2003; Chini et al. 2004; Beuther et al. 2004). The mass distribution of protostellar clumps in high-mass star forming regions also appears to be consistent with the stellar initial mass function (Beuther & Schilke 2004), strongly supporting accretion as the dominant mechanism for forming high-mass stars.

The molecular cloud bordering the large H II region NGC 7538 to the SE is known to contain several centers of active and on-going high-mass star formation (Werner et al. 1979; Kameya et al. 1989, 1990; Davis et al. 1998; Sandell & Sievers 2004). In the following we have adopted the distance to NGC 7538 as 2.8 kpc (Crampton, Georgelin & Georgelin 1978), which is the most commonly used distance estimate, although we note that two photometric studies (Beetz et al. 1976; Moreno & Chavarría-K 1986) place NGC 7538 at a distance of 2.2 kpc. NGC 7538 IRS 9, henceforth called IRS 9, is a deeply embedded cold IR source with a luminosity, $L \sim 4 \cdot 10^4 L_{\odot}$. IRS 9 is located $\sim 2'$ SE of the well studied Hyper Compact H II region IRS 1. The source is associated with a large reflection nebula (Werner et al. 1979; Eiroa, Lenzen & Gomez 1988; Tamura et al. 1991), drives a powerful extreme high velocity outflow (Kameya et al. 1989; Mitchell & Hasegawa 1991; Hasegawa & Mitchell 1995), and shows only weak free-free emission (Kameya et al. 1990), suggesting that it has not yet developed an H II region. There are several indications that IRS 9 may not be the only young stellar object in the IRS 9 cloud core. Deep CCD imaging (Campbell & Persson 1988) in r, i, and z filters revealed a diffuse nebula $\sim 50''$ W of IRS 9, which they identified as an HH object. Davis et al. (1998) found several knots of shocked H₂ emission at 2.12 μm , including a 40'' collimated jet. Neither the HH object nor the H₂ jet appear to point back towards IRS 9, suggesting that these are powered by other active young stellar objects embedded in

the IRS 9 molecular cloud core.

In this paper we present high angular resolution spectral line and continuum imaging of NGC 7538 IRS 9 with BIMA at 3.4 mm. We also present deep continuum imaging at 3.6 cm and additional data obtained from the VLA archive. Images in HCO^+ $J=2\rightarrow 1$ show that IRS 9 drives a compact bipolar high velocity outflow observed almost pole on. By re-analyzing published CO $J=2\rightarrow 1$ data together with our HCO^+ data, we detect at least two additional molecular outflows. One coincides with the H_2 jet and is highly collimated (axial ratio ~ 9) in blue-shifted HCO^+ emission. The second outflow is located in the dense cloud core south of IRS 9 and crosses the H_2 jet. We derive properties of the outflows and discuss what this implies for the star formation activity in the seemingly isolated IRS 9 cloud core.

2. Observations and Data Reduction

2.1. BIMA Observations

The observations of NGC 7538 IRS 9 were made in 2003 April and 2004 January using one frequency setting in the C and B-array configuration of the BIMA array resulting in a synthesized beam of $\sim 6''$. The correlator was split into four 25 MHz bands giving a velocity resolution of $\sim 0.34 \text{ km s}^{-1}$. We observed $\text{H}^{13}\text{CN } J=1\rightarrow 0$, $\text{SO } 2_2 \rightarrow 1_1$ and $\text{NH}_2\text{D } 1_{11} \rightarrow 1_{01}$ in the lower sideband of the first LO and $\text{HCO}^+ J=1\rightarrow 0$ in the upper sideband.

The data were reduced and imaged in a standard way using MIRIAD software (Sault, Teuben & Wright 1995). Phase calibration was applied using observations of the quasar 0102+584 at intervals of 30 minutes. The phase calibrator was observed using an 800 MHz bandwidth for 3 min. 3C454.3 was observed for 10 minutes as a bandpass calibration. The flux density scale was based on observations of Mars. The uncertainty in the absolute amplitude scale $\sim 15\%$, but the relative amplitude of spectral lines within the same receiver tuning is $\sim 5\%$.

The data were imaged with weighting inversely proportional to the variance in order to obtain the best signal to noise ratio. Averaging 4 spectral channels we obtained an RMS noise level of 40 mJy (0.2 K) with a synthesized beam Full Width Half Maximum (FWHM) of $6''.4 \times 4''.9$ at a position angle (p.a.) of -67° with a peak sidelobe level of -7% . Spectral windows which did not contain any significant spectral line emission were averaged to provide a continuum image with an RMS $\sim 3.5 \text{ mJy beam}^{-1}$. The continuum emission was subtracted from the spectral line channels, and the images deconvolved using the CLEAN algorithm.

2.2. VLA Observations and Archive Data

We carried out 3.6 cm continuum observations of NGC 7538 with the Very Large Array (VLA) of the National Radio Astronomy Observatory (NRAO)¹ in the BnA configuration on 2003 October 14. The effective bandwidth was 100 MHz with two circular polarizations. The pointing center was chosen half way between NGC 7538 - IRS 1 and NGC 7538 S, which gave us a good coverage of the whole NGC 7538 molecular cloud. The on source integration time was 1.3 hrs. We used 2229+5695 as the phase calibrator and 3C 48 for flux density calibration. The data were edited and calibrated using the AIPS software package. We estimate the absolute calibration accuracy to be $\sim 5\%$. The synthesized beam FWHM was $1''.21 \times 0''.47$, (p.a. = $+0^\circ$). The RMS noise in the vicinity of IRS 9 was $\sim 60 \mu\text{Jy beam}^{-1}$.

We have additionally searched the VLA data archive for any observations which may provide some further insight on the star formation activity in the IRS 9 region. We have re-reduced a 6 cm and 18 cm VLA run of NGC 7538 in the B array on 1989 April 28². The 6 cm track was a continuum track using 50 MHz bandwidth and the same phase calibrator and flux density calibrator (2229+5695 & 3C 48) as our 3.6 cm observations. The on source time was 2.7 hrs and the synthesized FWHM was $1''.35 \times 1''.09$ (p.a. -24°) with an RMS noise $\sim 100 \mu\text{Jy beam}^{-1}$ in the vicinity of IRS 9. The 18 cm run was configured for observations of 1665, 1667 and 1720 MHz OH maser emission with 127 channels and a bandwidth of 781.25 kHz corresponding to a velocity resolution of 0.55 km s^{-1} . We only searched for maser emission in the central half of the band, i.e. over a velocity range of -90 to -30 km s^{-1} . The synthesized beam for these observations was $4''.2 \times 3''.2$ (p.a. $+32^\circ$) and the RMS noise was 13 mJy beam^{-1} in the line data. We also found some short H₂O observations carried out on 29 January 2001 in the D to A array. The synthesized beam for these observations was $2''.36 \times 0''.38$ (p.a. 0°). The bandwidth for these observations was 3.125 MHz corresponding to a frequency resolution of 24.4 kHz (127 channels). The noise in line free channels was $\sim 27 \text{ mJy/beam}$. In this case we estimate the calibration accuracy to be no better than 20%.

We re-reduced some snapshot CH₃OH $7_0 \rightarrow 6_1 \text{ A}^+$ observations from 17 September 2001 at 44 GHz, which show a class I methanol maser in the vicinity of IRS 9 (Schwartz & Pratap 2002). The synthesized beam was $1''.8 \times 0''.76$ (p.a. $+53^\circ$). The velocity resolution for these observations was 0.4 km s^{-1} and the velocity coverage was 30 km s^{-1} . The RMS noise was $40 - 55 \text{ mJy beam}^{-1}$ in line free channels.

¹The NRAO is a facility of the National Science Foundation operated under cooperative agreement by Associated Universities, Inc.

²This is project AK224 referred to by Kameya et al. (1990)

2.3. JCMT Archive Data

We retrieved the CO J=2→1 data obtained with the James Clerk Maxwell Telescope (JCMT) on Mauna Kea, Hawaii, on 1997 June 2 & 3 from the JCMT archive at CADC³; see Davis et al. (1998) for a more detailed description. This observation was an on-the-fly map of the whole NGC 7538 molecular cloud scanned at a position angle of -45° sampling every $7''$ in the scan direction and stepping $10''$ between scans. The integration time per point was 12 seconds. Due to the sparse sampling the beam is somewhat broadened in the scan direction. We estimate the HPBW to be $\sim 22'' \times 21''$. The velocity resolution was 0.49 km s^{-1} and the velocity coverage was 650 km s^{-1} (500 MHz bandwidth). The data were reduced with SPECX and then exported to MIRIAD for further analysis. For the majority of the scans we only subtracted a linear baseline, but some of the scans taken towards the end of the run had poorer baseline quality. For these scans we used a fifth order polynomial, which resulted in flat baselines. The final map has an RMS of 1.5 K km s^{-1} in T_{mb} .

We also found some long integration H₂CO data of good quality taken on 1995 November 4. The H₂CO $3_{2,2} - 2_{2,1}$ transition at 218.47564 GHz and the $3_{0,3} - 2_{0,2}$ transition at 218.22219 GHz were observed simultaneously in a 500 MHz wide band, giving a velocity resolution of $\sim 0.48 \text{ km s}^{-1}$. The ratio of these H₂CO transitions is a good temperature probe for cold or moderately hot gas (Mangum & Wootten 1993). The integration time towards IRS 9 was 1980 sec, resulting in an RMS of 0.11 K in T_{mb} . The same data set also had an even longer integration, 3,000 sec, at the position ($+12''$, $-35''$) relative to IRS 9. The noise level of this spectrum is 0.08 K.

3. Continuum results

The deep 3.6 cm VLA observations with an angular resolution of $1''.21 \times 0''.47$ show a clear detection of a faint, marginally resolved source centered on IRS 9 (Table 1). There are no other sources within $100''$ of IRS 9. At 6 cm the free-free emission from IRS 9 is only a $3\text{-}\sigma$ detection. However, since the 6 cm emission agrees well in position with the 3.6 cm emission, we consider it to be reliable. The flux density at 6 cm is comparable to the 3.6 cm data, suggesting a flat spectral index. Such a flat spectral index is also found for the protostar NGC 7538 S (Sandell et al., in preparation) and most likely due to free-free emission from a well-collimated ionized wind (Reynolds 1986).

³Guest User, Canadian Astronomy Data Center, which is operated by the Dominion Astrophysical Observatory for the National Research Council of Canada's Herzberg Institute of Astrophysics

At 3.4 mm we find the continuum emission from IRS 9 to be a point-source surrounded by weak extended emission. The continuum peak agrees extremely well with our VLA position (Fig. 1, Table 1). Since the free-free emission is very weak and has a spectral index ~ 0 , essentially all the emission at 3.4 mm must arise from thermal dust emission. The observed size of the dust emission is about twice as large as Sandell & Sievers (2004) determined from single dish observations at 1.3 mm, 850 and 450 μm , suggesting that most of the dust emission at 3.4 mm originates from the dense cloud core in which IRS 9 is embedded. We note that our results disagree with the results reported by van der Tak et al. (2000), who found the dust emission to be unresolved in high spatial resolution ($\sim 2''$ beam) OVRO observations at 107 and 115 GHz (Table 1). Their flux densities, 43 and 95 mJy, at 107 and 115 GHz, respectively, are at least a factor of two higher than the current BIMA observations. If we extrapolate from the results quoted by Sandell & Sievers, who derived a dust emissivity index, $\beta \sim 2$, the single dish observations predict a integrated flux density of ~ 18 mJy, much less than our integrated flux density of 85 mJy at 3.4 mm (Table 1). The β -index derived by Sandell & Sievers (2004) is therefore likely to be overestimated. Most protostellar sources have an apparent β -index of 1 to 1.5 (Shirley et al. 2000), and a β -index of ~ 2 is not expected. In the following we assume that the β -index is 1.5.

If we assume that the dust emission is optically thin and that the bulk of the gas is at an average temperature, T_d , the total mass of gas and dust, M , can be expressed as $M = S_\nu D^2 / (\kappa_\nu B_\nu(T_d))$. Here $B_\nu(T_d)$ is the Planck function, κ_ν is the dust mass opacity, D is the distance, and S_ν is the integrated flux density at the frequency ν . For $\beta = 1.5$ and a gas to dust ratio of 100 we get $\kappa_{87} = 0.002 \text{ cm}^2 \text{ g}^{-1}$ (Hildebrand 1983). A dust temperature, T_d of ~ 40 K seems to be appropriate, based both on the results by Sandell & Sievers (2004) and the average gas temperature in the vicinity of IRS 9, which is ~ 30 K (Hasegawa & Mitchell 1995). With these assumptions we find a total mass from the 3.4 mm dust emission of $\sim 180 M_\odot$. If the β -index was as high as 2, the mass would be about four times larger. Since we find that IRS 9 drives a well-collimated molecular outflow (Section 5), we assume that IRS 9 is surrounded by an accretion disk. In this case the disk is most likely represented by the unresolved point-source emission at 3.4 mm (~ 8 mJy), and not by the extended emission, which originates from the surrounding dense cloud envelope. Our continuum observations therefore predict a disk-mass of $\sim 20 M_\odot$. This estimate is quite uncertain, both due to the uncertainty in the flux density assigned to the disk, and because of the limited knowledge of the dust properties and dust temperature of the proposed disk.

4. Molecular Cloud Cores - H¹³CN and SO emission

H¹³CN J=1→0 and SO 2₂ → 1₁ are good tracers of high density gas, i.e. densities ≥ 10⁵ cm⁻³. H¹³CN is a chemically robust molecule, i.e. its abundance is not strongly affected by shocks or temperature conditions. The emission should be optically thin and therefore provide an accurate image of the column density distribution of a dense molecular core as long as the gas temperature is fairly constant in the core. SO, although quite abundant in molecular clouds, often shows a different column density distribution relative to other high density tracers, presumably due to chemical effects (Swade 1989). The SO abundance is also enhanced in molecular outflows (Plambeck et al. 1982; Chernin et al. 1994), and can be significantly enhanced even in low-velocity shocks (Mitchell 1984).

HCO⁺ traces somewhat lower gas densities, ~ 10⁴ cm⁻³, than H¹³CN and is expected to be optically thick. It is therefore not a reliable column density tracer, at least not for the very dense molecular cloud cores that surround young high-mass stars. Furthermore the HCO⁺ abundance is often enhanced in high-velocity outflows (Mitchell & Hasegawa 1991), and the high velocity gas may completely dominate, as is the case towards IRS 9, see Section 5.

NH₂D 1₁₁ → 1₀₁ traces primarily cold, pristine molecular gas (Shah & Wootten 2001). Sandell et al. (2005, in preparation) have detected NH₂D in the NGC 7538 molecular cloud towards the high-mass protostar NGC 7538 S and in the dust filaments east and west of NGC 7538 S. No NH₂D emission is detected in the molecular cloud core near IRS 9; the IRS 9 core is therefore not likely to have a significant amount of cold, pristine gas.

Our observations show several regions of dense gas in the IRS 9 field (Fig. 2). There is an extended cloud core SE of IRS 9. The star itself is embedded in a “compact” cloud core almost detached from the larger cloud. To the west, near the edge of our primary beam, there is a region of very strong, narrow SO emission. High resolution images of NH₃ (Zheng et al. 2001) show a very similar distribution, except that NH₃ is largely absent towards IRS 9, whereas we detect the strongest H¹³CN emission towards IRS 9.

4.1. The IRS 9 Cloud Core

The H¹³CN and SO emission peak within ~ 1'' of IRS 9. The SO emission appears more compact, and shows a fainter secondary peak ~ 5'' W of IRS 9 (Fig 2). The size of the H¹³CN emission, excluding high velocity gas, is ~ 18'' × 8'' extending EW, i.e. similar to the extent of the dust emission at 3.4 mm (c.f. Section 3). The radial velocity determined from the main hyperfine transition of H¹³CN (F =2 → 1) , ~ -57 km s⁻¹, agrees well with

that determined from observations of a number of transitions of CS and H₂CO (van der Tak et al. 2000). We resolve the hyperfine structure in H¹³CN and in addition to the F = 2 → 1 transition we also observe the upper hyperfine transition, F = 1 → 1 (Fig. 3), which for optically thin emission has a line intensity of 0.6 times the F = 2 → 1 line. The F = 0 → 1 hyperfine component may also be present, but is generally weak (~ 0.2 times the intensity of the F = 2 → 1 transition for optically thin emission). Since the F = 1 → 1 hyperfine transition is only separated by +4.9 km s⁻¹ from the F = 2 → 1 transition, the two lines often appear partially blended. We observe no obvious velocity gradient in either H¹³CN or SO. Both H¹³CN and SO show high velocity wings (Fig. 3), confirming that the extreme high velocity outflow driven by IRS 9 has very high densities, at least at low and moderate velocities. The high velocity emission completely dominates in HCO⁺ (Fig. 3), which will be discussed in more detail in Section 5.1.

The single dish JCMT H₂CO data (Fig. 4) give $T_{mb}(3_{0,3} - 2_{0,2})/T_{mb}(3_{2,2} - 2_{2,1}) = 3.5 \pm 0.3$, integrated over the central 3 km s⁻¹, suggesting a gas temperature ≥ 60 K (Mangum & Wootten 1993). However, Hasegawa & Mitchell (1995) derive a lower temperature of 32 ± 8 K from analysis of the J=3→2 and J=4→3 transitions of HCO⁺ and H¹³CO⁺, while Mitchell et al. (1990), using absorption lines of the fundamental vibrational band of ¹³CO at 4.7 μm, derived 26 K. The latter two studies therefore suggest that the temperature of the dense gas surrounding IRS 9 is ~ 30 K, while the H₂CO data suggest a substantially higher temperature. The other position observed in H₂CO, at (+12'', -35'') in the southern cloud core gives $T_{mb}(3_{0,3} - 2_{0,2})/T_{mb}(3_{2,2} - 2_{2,1}) = 7.0 \pm 0.4$, corresponding to a gas temperature of ~ 30 – 35 K, in good agreement with the temperature derived by Hasegawa & Mitchell (1995) from HCO⁺ data at the same position. However, since both H₂CO transitions show clear line wings towards IRS 9, the emission from the hot outflow at near-cloud velocities add a substantial contribution to the line integral, causing an incorrect line ratio for the core emission. If we fit the H₂CO spectra with a two-component Gaussian, one for the cloud emission and one for the broad wing emission, we find that a ratio of ~8 for the cloud core, corresponding to an average gas temperature of 30 K. In the following we adopt 30 K as the excitation temperature for H¹³CN, resulting in a column density towards IRS 9 of ~ 3.6 10¹³ cm⁻². If we assume an abundance ratio for HCN similar to the OMC-1 extended ridge (Blake et al. 1987), i.e. [HCN]/[H₂] = 5 10⁻⁹, and an isotope ratio, [¹²C]/[¹³C] = 85 (Wilson & Rood 1994), we find a total H₂ column density of 6.1 10²³ cm⁻² towards IRS 9. If we assume that the relationship between color excess and total hydrogen column density (Bohlin et al. 1987) is valid also for dense molecular gas, the observed column density suggests that IRS 9 is obscured by a visual extinction of more than 300^m, yet Tielens et al. (1991) derived a visual extinction of only ~ 75^m from observations of the CO absorption band at 4.67 μm. These two estimates are not necessarily discrepant, because as we will show in Section 5.1,

IRS 9 drives a well collimated high velocity outflow observed almost pole-on, clearing away enough of the foreground cloud to allow the star to be detectable in the near IR.

If we integrate the H^{13}CN emission over the IRS 9 cloud core we derive a total mass $\sim 350 M_{\odot}$. This mass estimate is in good agreement with the value based on our continuum observations, $180 M_{\odot}$ (Section 3), especially considering that the the abundance ratio of $[\text{H}^{13}\text{CN}/\text{H}_2]$ is uncertain by at least a factor of two or three. Our observations therefore show that IRS 9 is still surrounded by a very dense cloud core with a mass of $\geq 100 M_{\odot}$.

4.2. The cloud core SE of IRS 9

The molecular cloud core SE of IRS 9 dominates the emission in H^{13}CN and SO . The core has a diameter of $\sim 40''$ and shows several emission peaks. H^{13}CN shows a ridge of emission in p.a. $\sim 25^\circ$, with a strong peak at an offset $\sim (6'', -22'')$ from IRS 9 (Fig 2). Another extended emission peak is observed at the SE boundary of the H^{13}CN cloud and is also distinctly visible on the $450 \mu\text{m}$ SCUBA image (Fig. 6). It is barely detected in SO , which otherwise exhibits a similar morphology (Fig. 2). Both H^{13}CN and SO show red- and blue-shifted wings towards the dominant emission peak at $(6'', -22'')$ (Fig 3), while HCO^+ shows deep red-shifted self-absorption. Even H^{13}CN is strongly affected by self-absorption. Strong red-shifted self-absorption in HCO^+ is usually interpreted as evidence for infall or accretion towards a central protostellar object. Since we also observe a bipolar outflow originating from this position (Section 5), there must be a young protostar deeply embedded in this cloud core. A Gaussian fit to the H^{13}CN peak gives a size of $14'' \times 6''$ (p.a. $\sim 20^\circ$). If we assume the same gas temperature and H^{13}CN abundance as used for the cloud core surrounding IRS 9, a mass of $> 250 M_{\odot}$ for the compact cloud core surrounding the protostar is suggested. This is a lower limit, since we have made no correction for the self-absorption, which virtually blocks all emission at the cloud velocity (Fig 5). The average gas density of this protostellar core is therefore $> 6 \cdot 10^6 \text{ cm}^{-3}$. The large cloud core, in which this protostellar core is embedded, has a mass of $> 900 M_{\odot}$, providing a large mass reservoir for additional star formation.

We have have examined the H^{13}CN and SO data to see if there is any evidence for a rotating disk, which would be expected around such a young, heavily accreting protostar. However, based on the position velocity plot in Fig. 5, the dense surrounding cloud core effectively obscures the protostar; it is thus impossible to observe the central protostar in these molecular transitions. An improved “disk probe” is therefore required, which is not obscured by the cold cloud envelope or the outflow, which may mask any kinematics of the disk.

Such a disk maybe observable in CH₃CN or in higher rotational transitions of H¹³CN or DCN. However, since one can see high velocity emission from the dense outflow in H¹³CN J=1→0, and since the outflow appears to be hot (Sect. 5.5.1), the outflow is likely to dominate, making H¹³CN a poor choice. DCN is usually not seen in outflows, but appears to be a good disk tracer (Sandell et al. 2005, in prep.) and may therefore be a better choice than H¹³CN.

4.3. The sub-mm source IRS 9 S

H¹³CN and SO avoid IRS 9 S, the southern sub-mm source, which Sandell & Sievers (2004) suggest might host another protostar. Both H¹³CN and SO seem to form almost a semi-shell around the eastern boundary of this sub-mm source (Fig. 6). The absence of molecular emission from IRS 9 S is puzzling. One possibility is that this is an extremely dense, cold protostellar core, in which most molecules are frozen onto interstellar dust. However, if this is the case, we would expect to see NH₂D emission, which is absent. If IRS 9 S were a cold source, strong emission strong source at 1.3mm and 850 μm is expected. However, Sandell & Sievers (2004) found it to be faint at these wavelengths. The other possibility is that IRS 9 S is a hot source. We note that Zheng et al. (2001) detected NH₃ towards IRS 9 S, and remark that the NH₃ emission shows larger velocity dispersion and higher optical depth than the emission in the vicinity of IRS 9. A plot of the line ratios of the (J,K) inversion transitions (2,2) and (1,1) presented by Zheng et al. (2001) indicates that the gas is hotter towards IRS 9 S. A dense hot ($T_R \geq 80$ K) core is a more likely explanation. Yet the source of energy for such a hot core is unknown, since we detect no free-free emission at 3.6 cm to a limit of 60 μJy beam⁻¹, nor is any outflow or maser emission present in the core.

5. High velocity outflows and masers

The BIMA HCO⁺ J=1→0 spectrum towards IRS 9 shows broad line wings (Fig. 3); we have not even observed the full extent of the high velocity emission in our 25 MHz band, corresponding to a velocity range of 90 km s⁻¹ (–94 to –11 km s⁻¹). The broad line wings are no surprise, since IRS 9 is known to power an extreme high velocity CO outflow (Mitchell & Hasegawa 1991), which is also very prominent in HCO⁺ (Hasegawa & Mitchell 1995). The extreme high velocity emission is only observed in the vicinity of IRS 9, although there is widespread high velocity gas in the IRS 9 molecular core (Kameya et al. 1990; Mitchell & Hasegawa 1991) and several regions of shocked H₂ emission including a well collimated jet (Davis et al. 1998). Kameya et al. (1989) noticed that the high velocity gas ~ 30'' SE of

IRS 9 showed both blue- and red-shifted emission, suggesting that this gas could be part of a separate outflow. Davis et al. (1998) also suggested that multiple outflows exist in the IRS 9 region.

In the following we will use our high spatial resolution HCO^+ $J=1\rightarrow 0$ BIMA images together with images of shocked $2.12\ \mu\text{m}$ H_2 and single dish CO $J=2\rightarrow 1$ images from Davis et al. (1998), to show that there are at least three separate high velocity outflows in the IRS 9 region, all partially overlapping with each other. The occurrence of H_2O , 1720 MHz OH , and class I CH_3OH masers, which are excited in these outflows, provide additional information in identifying the various outflows. The H_2O masers, which may be excited in the accretion disks powering the outflows, provide further evidence on the location of the stars driving the outflows.

To obtain a better overview of the distribution of the high velocity gas, we use four sets of images of HCO^+ and CO (Fig 7), where we partitioned the blue- and red-shifted high velocity gas into four velocity regimes: *i)* low velocities, *ii)* intermediate velocities, *iii)* high velocities, and *iv)* extreme velocities. The first three sets are all integrated over $6.5\ \text{km s}^{-1}$ wide velocity intervals for both HCO^+ and CO . We begin at velocities of $\pm 5\ \text{km s}^{-1}$ from the cloud core to avoid emission from turbulent gas in the ambient cloud. For the extreme high velocity emission we begin at velocities $\pm 25\ \text{km s}^{-1}$ from the cloud velocity and integrate to the highest velocities detected. These contour images of blue- and red-shifted emission are shown in Fig. 7.

Using the HCO^+ (and CO) images we identify three outflows: *i)* The extreme high velocity HCO^+ emission shows a compact bipolar outflow centered on IRS 9 (the IRS 9 extreme high velocity outflow), *ii)* At low and intermediate velocities, HCO^+ shows a highly collimated blue-shifted outflow well aligned with the H_2 jet at a p.a. of 155° with no red-shifted counterpart (the H_2 jet), and *iii)* a poorly collimated blue-shifted outflow with a compact red-shifted counterflow at p.a. $\sim 28^\circ$ (the protostellar outflow). The last outflow intersects with the H_2 jet $\sim 24''$ south of IRS 9. In the following we discuss each outflow in more detail, adding information from the CO images, the maser observations and images of high density gas based on H^{13}CN and SO , which were discussed in Section 4.

5.1. The IRS 9 extreme high velocity outflow

The HCO^+ data show that IRS 9 drives a bipolar extreme high velocity outflow approximately oriented EW. The center of symmetry is within $1''$ of IRS 9 (Fig. 7). The outflow is very compact and highly collimated; the extent of the outflow lobes are $\sim 14''$. The two H_2O

maser spots (Table 2) detected by Kameya et al. (1990) are centered close to the VLA continuum source. Both are blue-shifted relative to the cloud velocity and are probably excited in the outflow close to the stellar disk. We also observe two CH₃OH masers, one close to the star and one in the blue-shifted outflow lobe. Both have velocities close to the systemic velocity. We also detect a slightly red-shifted 1720 MHz OH maser in the red-shifted outflow lobe. Davis et al. detected two bright H₂ knots west of IRS 9. Both lie in the blue-shifted outflow lobe at $\sim (-9''.1, -3''.6)$ and $(-16''.6, -2''.5)$ relative to IRS 9, suggesting that they are excited by the high velocity gas in the blue-shifted outflow. Since the outflow lobes of the IRS 9 outflow are largely overlapping, the HCO⁺ observations suggest that the extreme high velocity outflow is observed nearly pole on. If we assume that the ellipticity of the outflow lobes is caused by projection, the outflow is inclined by $\sim 20^\circ$ to the line of sight. Observing the outflow pole on explains why the IRS 9 outflow shows such extreme high velocities. Mitchell & Hasegawa (1991) found that the red-shifted outflow has an outflow velocity of 110 km s⁻¹ in CO J=3→2, while the blue-shifted outflow wing was much less prominent and has a velocity span of only 40 km s⁻¹. In the single dish CO J=2→1 images (Fig. 7), the outflow is severely blended with the two other outflows and the bipolar nature is not at all evident. At the position of IRS 9, however, the CO high velocity wings extend from ~ -80 to $+20$ km s⁻¹ in V_{lsr} , with a strong red-shifted wing and a much fainter blue-shifted wing. In HCO⁺ the blue- and red-shifted outflow wings are largely symmetrical (Fig. 3). The approximate symmetry of the two outflows lobes is clear in the position velocity plot taken along the symmetry axis of the outflow (Fig. 8).

Since our observations show that the outflow is much more compact than previously believed, it is also much younger. If we use the observed maximum velocity of 110 km s⁻¹ (Mitchell & Hasegawa 1991) and assume 20'' as the total extent of the outflow (~ 0.8 pc), we find a dynamical timescale of ~ 6600 yr for the red outflow lobe. The large mass outflow and youth of the IRS 9 outflow suggests that IRS 9 is still in an active accretion phase. Even though the outflow is observed almost pole on, and the outflow therefore largely masks any infall signature, a narrow absorption in the redshifted outflow lobe is detected (Fig. 3), most likely arising from cold infalling gas (see Section 6.2).

5.2. The H₂ jet

The narrowband 2.12 μ m H₂ imaging by Davis et al. (1998) shows a highly collimated H₂ jet terminating $\sim 60''$ S of IRS 9. As we have already discussed, this jet is not powered by IRS 9, because the high spatial resolution HCO⁺ imaging shows that IRS 9 drives a compact nearly pole-on bipolar outflow. At intermediate blue-shifted velocities HCO⁺ shows an

extremely well collimated outflow at a p.a. $\sim 155^\circ$, which coincides with the H_2 jet (Fig. 7). This outflow is also observed in CO, where it dominates the high velocity emission at all blue-shifted velocities (Fig. 7). With a $22''$ resolution, the outflow blends in with the IRS9 outflow, giving the appearance that it is powered by IRS9. The CO images also show a prominent red-shifted counter jet NW of IRS9 extending to $\sim 50''$ N of IRS9. This red-shifted outflow lobe has no obvious counterpart in HCO^+ . At low and intermediate velocities, faint red-shifted HCO^+ emission coinciding with the cluster of H_2 knots $\sim 50''$ N of IRS9 and at $(\sim -30'', +20'')$ (Fig. 9) is observed. Both of these compact red-shifted HCO^+ knots lie in the outskirts of the red-shifted CO lobe and coincide with regions of high gas density. At both positions where we observe HCO^+ high velocity emission N of IRS9, we also detect H^{13}CN emission.

At low velocities a compact red-shifted emission peak slightly north of the methanol maser IRS9- $\text{CH}_3\text{OH}(3)$ (Fig. 7) is obvious. This red-shifted emission peak is close to the protostellar source at $(6'', -22'')$. This coincidence is seen more clearly in Fig. 9, where we overlaid the HCO^+ emission integrated over low and intermediate velocities on the map of integrated H^{13}CN emission. The CO image, however, shows that this red-shifted HCO^+ emission peak coincides with a red-shifted CO outflow extending to the SW rather than to the N. The red-shifted HCO^+ emission therefore appears to be part of the protostellar outflow. The source of the blue-shifted HCO^+ may reside in the protostellar core. However, more likely the source of the outflow lies in the IRS9 cloud core, since we observe high velocity blue-shifted HCO^+ emission between the protostellar core and IRS9. The $2.12\ \mu\text{m}$ H_2 image shows a nebulous IR source at an offset of $(-2''.2, -1'')$ from IRS9, labeled as peak A1 by Tamura et al. (1991), who interpreted it as a peak in the reflection nebula. We believe it may be another embedded young star and therefore a potential exciting source for the HCO^+ jet.

This outflow looks very similar to the IRS9 outflow, if we account for the difference in inclination. Both outflows are very highly collimated and jet-like and similar in size. The CO map shows a maximum velocity of $\sim 50\ \text{km s}^{-1}$ for the blue-shifted H_2 jet. This velocity may be a lower limit, since the CO image does not cover the full extent of the blue outflow lobe; a position velocity plot of CO along the outflow shows that the outflow is accelerating, i.e. the highest outflow velocities are observed at the tip of the outflow. The same behavior is seen in HCO^+ , but the maximum velocity in HCO^+ is lower by $\sim 25\ \text{km s}^{-1}$. The velocities are somewhat lower in the red-shifted outflow, where CO shows a maximum velocity of $\sim 37\ \text{km s}^{-1}$. The outflow is quite extended, $\sim 50'' - 70''$, depending on whether we assume that the driving source lies in the protostellar core or in the IRS9 core.

5.3. The protostellar outflow

At extreme velocities (Fig. 7) faint blue-shifted HCO^+ emission extending from the southern H^{13}CN peak to the NE (p.a. $\sim 28^\circ$) is observed. The maximum velocity of the blue-shifted HCO^+ outflow is $\sim 28 \text{ km s}^{-1}$. At lower velocities the outflow lobe merges into the outflow tracing the H_2 jet and appears less collimated. At low velocities HCO^+ shows a more compact lobe of red-shifted emission, which is well aligned with the symmetry axis of the blue-shifted emission. The intercept between red- and blue-shifted emission is roughly at the position of the southern H^{13}CN peak (Fig. 9). However, the red-shifted HCO^+ emission is also approximately on the symmetry axis of the H_2 jet, and could therefore also be associated with the H_2 jet.

In the low spatial resolution CO maps the blue-shifted emission is completely blended with the outflow associated with the H_2 jet. The only appearance of this rather compact blue-shifted HCO^+ outflow in CO is that the blue CO wing covers a larger velocity range ($\sim 35 \text{ km s}^{-1}$) at the position of the protostar and the blue outflow lobe widens up and curves to the N just S of IRS9. The red-shifted counter flow, which is very compact in HCO^+ , is clearly visible in CO at moderate and high velocities. At higher velocities the red-shifted emission lobe appears to be shifted to the N (Fig. 7). It is therefore possible that what we identified as the symmetry axis of the blue-shifted outflow is the northern wall of the outflow. An outflow with a p.a. of 60° , and a poorly collimated blue outflow lobe with an opening angle of $50^\circ - 60^\circ$ is also plausible. Such an outflow geometry could explain why we observe high velocity gas at the SW boundary of the H^{13}CN core, which in this scenario would represent the southern outflow wall of the outflow.

As we already noted in Section 4.2, the southern H^{13}CN peak at ($6'', -22''$) shows high velocity wings in both H^{13}CN and SO (Fig. 3), suggesting that there is a YSO embedded in the core driving a high velocity outflow. This YSO appears to be a protostar, since HCO^+ shows deep red-shifted self absorption, presenting strong evidence for infall (Section 6.2). The emission from dense high velocity gas traced by H^{13}CN places the protostellar source right between the red- and the blue-shifted outflow lobe (Fig. 10), confirming that the protostellar source drives this rather compact outflow, which in the blue-shifted outflow lobe only extends $\sim 25'' - 30''$ from the driving source terminating near the eastern red-shifted outflow lobe from IRS9.

The protostellar outflow shows deceleration, i.e. the highest outflow velocities are seen towards the center of the outflow. In this respect it looks very similar to the very young compact outflow driven by NGC 7538 S (Sandell, Wright & Forster 2003). If molecular outflows from high-mass protostars are driven by jets, one would expect to see deceleration when the outflow is very young and has not yet had time to accelerate the gas in the

surrounding dense cloud core. This outflow may therefore be even younger than the IRS 9 outflow, even though its dynamical timescale is about the same or larger than the IRS 9 outflow (Table 3). Both outflows are certainly very young.

5.4. Unexplained high velocity features

At low red-shifted velocities the CO map shows a tongue of emission extending to $\sim 50''$ west of IRS 9 (Fig. 7). This velocity feature is also seen in the CO $J=3 \rightarrow 2$ map by Mitchell & Hasegawa (1991). Although we can plausibly explain the shocked H_2 knots north of IRS 9 by assuming the red-shifted outflow is expanding more freely through the low density gas north of IRS 9, it cannot explain why the outflow would flow backwards. It is therefore likely that there is another outflow west or northwest of IRS 9. This outflow terminates (or originates) close to the HH object reported by (Campbell & Persson 1988), and would therefore provide the energy to excite this HH object. Our HCO^+ map also shows low velocity red- and blue-shifted emission at $\sim (-33'', -30'')$ in the southwestern part of the reflection nebula, which has the appearance of a compact bipolar outflow (Fig. 9). This outflow is not seen in CO, which makes it somewhat dubious. However, if the outflow is as compact and faint as indicated by our HCO^+ data, it would be difficult to see in the CO map, which does not go very deep.

5.5. Outflow characteristics

We derive the physical characteristics of the outflows following the recommendations and formulae presented in the careful study of outflow characteristics by Cabrit & Bertout (1992). Since we have images in both HCO^+ and CO we derive the outflow parameters by integrating over the same velocity intervals that we used for identifying the outflows, see Section 5. For correcting the outflow parameters for inclination, we assume a mean inclination of 57.3° , see e.g. Bontemps et al. (1996), except for the IRS 9 outflow, where we use 20° , as determined from the outflow morphology (Sect. 5.1). However, most of our information about the outflows comes from HCO^+ and since the HCO^+ abundance can be considerably enhanced in outflows (Garden & Carlstrom 1992; Hasegawa & Mitchell 1995), this could lead to large uncertainties in determining the mass of the high velocity gas. The IRS 9 outflow is also known to be very hot (Mitchell & Hasegawa 1991) and since the column density of a molecule is approximately linearly dependent on the gas temperature, the mass of an outflow can be seriously underestimated if the outflow temperature is assumed to be the same temperature as the surrounding molecular cloud; an assumption often made in

outflow studies (Shepherd & Churchwell 1996; Beuther et al. 2002). Below we discuss in more detail how we determined the temperature and the mass of the outflows, which have been used to derive most of the outflow parameters given in Table 3.

5.5.1. *Temperatures of the outflows*

Mitchell & Hasegawa (1991) used their CO J=3→2 and J=2→1 observations to deduce the gas temperature of the IRS9 high velocity outflow. They found the red-shifted gas to be very hot, ~ 200 K, while they deduced a much lower temperature for the blue-shifted gas, ~ 40 K. A later study (Hasegawa & Mitchell 1995), using several rotational transitions of HCO⁺, gave similar results. Mitchell et al. (1990) observed the fundamental vibrational band of CO and ¹³CO at 4.6 μ m in absorption against IRS9 and found a temperature of ~ 180 K, which is in good agreement with what Mitchell & Hasegawa (1991) found for the red-shifted outflow using the rotational CO emission lines. However, since the absorption studies must primarily sample the blue-shifted gas, there is an inconsistency between the hot temperature deduced from the absorption studies and the cold temperature deduced from emission lines. The apparent weakness of the blue-shifted CO wing compared to the red-shifted wing is easily explained if we assume that the hot gas in the blue outflow is self-absorbed against colder high velocity gas, see e.g. Beltrán et al. (2004). This explains not only the weakness of the blue-shifted outflow relative to the red-shifted outflow, but also why the emission lines produce an incorrect temperature for the blue-shifted outflow. The H₂CO 3_{2,2} – 2_{2,1} and 3_{0,3} – 2_{0,2} transitions only show weak line wings towards IRS9 (Fig. 4), but the wing emission is about equally strong in both transitions and very symmetric. A two component Gaussian fit to both spectra give the same radial velocity for both the cloud core and plateau (wing emission) resulting in a line ratio $T_{peak}(3_{0,3} - 2_{0,2})/T_{peak}(3_{2,2} - 2_{2,1}) = 1.9$ for the high velocity emission, strongly supporting the earlier conclusion that the gas is hot in both outflow lobes. If the blue-shifted outflow was as cold as 40 K, we would not see any blue-shifted wing in the 3_{2,2} – 2_{2,1} transition. For estimating outflow masses we will therefore adopt an excitation temperature of 180 K for the red- and the blue-shifted high velocity emission.

For the other two outflows we have far less information, but both appear colder than the IRS9 outflow. Hasegawa & Mitchell (1995) derived a temperature of 40 K for the position (+10", –35"), which is well centered on the blue-shifted jet, although within their 15"-beam, they also include some emission from the protostellar outflow. The spectra of the 3_{2,2} – 2_{2,1} and 3_{0,3} – 2_{0,2} transitions of H₂CO at the same position (Fig. 4) show strong blue-shifted wings in both transitions and the ratio of the wing emission integrated from –72 – –60

km s⁻¹, i.e. $T_{wing}(3_{0,3} - 2_{0,2})/T_{wing}(3_{2,2} - 2_{2,1}) = 3.13 \pm 0.06$, suggesting a temperature ≥ 80 K (Mangum & Wootten 1993), seemingly in conflict with the HCO⁺ results. However, in this case the H₂CO HPBW is larger, 22'', and the high velocity emission seen in H₂CO must originate from the protostellar outflow, not the H₂ jet, because only the protostellar outflow has outflow densities which are high enough to excite H₂CO in the outflow. For the H₂ jet we therefore adopt an outflow temperature of 40 K, while we use 80 K for the protostellar outflow.

5.5.2. Outflow masses

CO is a very good outflow tracer, but in high mass star forming regions which have massive turbulent envelopes, one can more easily see the outflow in high density tracers like SiO or HCO⁺. However, if the gas density of the surrounding cloud is low, the density of the entrained high velocity gas may not be high enough to excite HCO⁺ in the outflow, which is why we do not see the red-shifted outflow lobe of the H₂ jet, although it is quite prominent in CO. Neither will HCO⁺ trace high velocity gas at the very highest outflow velocities, because the entrained gas densities become too low to excite HCO⁺. Since most of the mass of an outflow is at low velocities, the mass of such high velocity gas is generally negligible compared to the total mass of the outflow, although it can still dominate the energetics of an outflow (Mitchell & Hasegawa 1991). The uncertainty of the HCO⁺ abundance causes much larger uncertainties in the outflow masses derived from HCO⁺. However, since we know the size of the outflow from our high-spatial resolution HCO⁺ imaging, we can use the single dish CO J=2→1 map to calibrate the HCO⁺ abundance. Since the blue-shifted CO outflow is anomalously weak due to self-absorption, we only use the red outflow, and avoid near-cloud velocities, where the CO emission is optically thick. If we integrate over the velocity range -46 km s⁻¹ to -10.5 km s⁻¹, we obtain a mass of $2.3 M_{\odot}$, assuming that CO is optically thin. Integrating HCO⁺ over the same velocity range and assuming that HCO⁺ is emitted from the same gas as CO, we obtain an HCO⁺ abundance, $[HCO^+/H_2] = 6 \cdot 10^{-8}$. This abundance is 30 times higher than the “standard” Orion ridge HCO⁺ abundance, $2 \cdot 10^{-9}$ (Blake et al. 1987). At extreme velocities, -10 km s⁻¹ – $+20$ km s⁻¹, the outflow mass derived from CO is very modest, $0.3 M_{\odot}$. At near cloud velocities, -52 km s⁻¹ – -46 km s⁻¹, it is more difficult to derive a CO mass, since CO is likely to be optically thick and the emission in this velocity range is dominated by emission from the background cloud at -49 km s⁻¹, see e.g. (Mitchell & Hasegawa 1991). The CO map shows that the emission from the background cloud is approximately uniform over the map and we can therefore correct for the emission from the cloud at -49 km s⁻¹, resulting in an optically thin mass of $1.7 M_{\odot}$. If we scale this mass by the mean opacity correction factor 3.5 derived by Bontemps

et al. (1996) for the sample of outflows compiled by Cabrit & Bertout (1992), we get an HCO^+ abundance $\sim 10^{-8}$. At low velocities the HCO^+ abundance therefore appears to be only slightly enhanced. The calibration of HCO^+ abundance relative to CO is still subject to some uncertainty, especially since we compare high spatial resolution HCO^+ data to CO, which is observed with a much larger beam ($22''$). The CO emission may therefore include emission from the H_2 jet and from low density high velocity gas, which is not dense enough to be collisionally excited in HCO^+ . For the IRS 9 outflow we adopt an $[\text{HCO}^+/\text{H}_2]$ abundance of 10^{-8} for the near-velocity gas and $6 \cdot 10^{-8}$ for high and extreme velocity gas, resulting in outflow masses, of $8.1 M_\odot$ and $7.8 M_\odot$ for the red and blue outflow, respectively (Table 3). The mass derived from HCO^+ is the same in both outflow lobes. The mass discrepancy seen in earlier observations can therefore be attributed to strong self-absorption of the hot blue-shifted high velocity gas against colder high velocity gas, which appears to affect CO much more strongly than HCO^+ .

For the other two outflows we cannot use CO to calibrate the HCO^+ abundance, since we see none, or only small amounts of red-shifted HCO^+ emission, and the blue-shifted outflow lobes cannot be separated in CO. For the mass estimates in Table 3, we have assumed that the HCO^+ emission has a normal abundance ratio, $[\text{HCO}^+/\text{H}_2] = 2 \cdot 10^{-9}$. Since the blue-shifted jet overlaps with the protostellar outflow even in our high spatial resolution HCO^+ observations, our mass estimates have somewhat larger uncertainties due to the difficulties in partitioning the high velocity emission between the outflows. The red-shifted outflows are well separated in CO, and here we have estimated the CO mass by spatially integrating the CO emission in the same velocity intervals we used for estimating the mass of the IRS 9 outflow. We have corrected the optically thin CO mass for near-cloud velocities with the same opacity correction (3.5) as we used for the IRS 9 outflow. The masses derived from CO for the red-shifted outflows agree within a factor of two with the blue-shifted outflow masses derived from HCO^+ (Table 3), supporting our assumption that for these outflows the HCO^+ abundance is not significantly enhanced.

6. Discussion and Conclusions

6.1. The IRS 9 molecular cloud is forming a cluster

The high spatial resolution BIMA observations show that the molecular cloud surrounding IRS 9 breaks up into two cloud cores, one surrounding IRS 9, and one SE of IRS 9. The SE cloud core appears to be fragmenting into further sub-condensations (Section 4). Observations of HCO^+ show three bipolar molecular outflows. The dynamical time scales for each outflow is $\sim 10^4$ yr, suggesting that they are all young. All three outflows have outflow

masses in the range 20 - 60 M_{\odot} and momentum fluxes $> 10^{-2} M_{\odot} \text{ km s}^{-1} \text{ yr}^{-1}$, which is more than a magnitude higher than observed for low-mass stars (Cabrit & Bertout 1992; Bontemps et al. 1996), but similar to values derived for outflows in other high mass star formation regions (Shepherd & Churchwell 1996; Henning et al. 2000; Zhang et al. 2001; Beuther et al. 2002). Although only one of the stars driving the outflows have detectable radio continuum, the outflow characteristics and high accretion rates (Section 6.2) suggest that they will all evolve into high-mass stars. It is very likely that there are more outflows in the IRS9 cloud than those we have identified. We observe high velocity features, which are difficult to explain with only three outflows, and we have additionally identified an H_2O maser, which does not coincide with any of the outflows. Since we have only imaged the high velocity gas in HCO^+ , which has a critical density of $\sim 10^4 \text{ cm}^{-3}$, we are only sensitive to very dense high velocity gas and many outflows, especially from low mass protostars, are not always detected in HCO^+ . Multiple outflows near high mass protostars appear to be common. Interferometer observations reveal multiple outflows in several regions of massive star formation: at least three outflows in IRAS 05358+3543 (Beuther et al. 2002), as many as four outflows from the core containing G 35.2–0.7N (Gibb et al. 2003), and seven to nine molecular outflows in the massive star-forming region IRAS 19410+2336 (Beuther, Schilke & Stanke 2003). The intermediate-mass region IRAS 20293+3952 has four molecular outflows, including one as highly collimated as the jet-like outflows observed in low-mass star formation sources (Beuther & Schilke 2004).

6.2. Evidence for accretion

Radiative transfer models show that accretion onto a young stellar object will result in self-absorbed asymmetric line profiles for optically thick lines, with the blue-shifted side of the line being stronger than the red-shifted one (Leung & Brown 1977; Zhou 1992; Zhou et al. 1993). If the brightness temperature of the continuum emission from the protostar exceeds the temperature of the infalling gas, gas in front of the star will appear in absorption, while the gas behind the star will be in emission, resulting in an inverse P Cygni line profile, and providing strong evidence for infall. Inverse P Cygni line profiles or line asymmetries consistent with a centrally condensed infalling cloud have been observed towards several massive star forming regions (Welch et al. 1987; Keto, Ho, & Haschick 1988; Zhang & Ho 1997; Zhang, Ho & Ohashi 1998). In the earliest stages of the formation of a massive protostar, the central core may be colder or about the same temperature as the infalling envelope. The line profiles will therefore be more symmetric or even stronger on the red-shifted side. However, if the massive protostar drives a hot molecular outflow, self-absorption may be observed against the high velocity gas.

Both IRS 9 and the southern protostar show red-shifted self-absorption against the hot HCO^+ outflows driven by these stars. Since IRS 9 drives an almost pole-on outflow, the outflow is expected to largely fill in any signature of accretion, and the self-absorption in HCO^+ is indeed much less pronounced than for the southern protostar (Fig. 3). Towards the southern protostar we observe a deep, narrow, $\sim 0.8 \text{ km s}^{-1}$ wide self-absorption feature with a broad, $\sim 4 - 5 \text{ km s}^{-1}$ red-shifted shoulder (Fig. 3). Examination of spectra and channels maps show that the narrow absorption feature is still detectable $\sim 7'' - 10''$ from the protostar, although it becomes even narrower in width, $0.5 - 0.8 \text{ km s}^{-1}$, while the fainter broad absorption is only detectable in the immediate vicinity of the protostar. At the position of the protostar the broad red-shifted absorption component is $\sim 8.9 \text{ K km s}^{-1} \text{ beam}^{-1}$, while the narrow component has an integrated intensity of $1.7 - 2 \text{ K km s}^{-1} \text{ beam}^{-1}$. Since the FWHM of the narrow component is $\sim 10''$, the total intensity is $7 - 8 \text{ K km s}^{-1}$. The integrated intensity of the observed self-absorption gives an estimate of the mass of the infalling gas. If we assume optically thin gas with a temperature of 30 K , the mass is $\sim 1.9 M_{\odot}$. This is a lower limit, since the optical depth of the infalling gas must be ≥ 1 to be seen in absorption. If we assume that the time scale for accretion is about the same as for the outflow, i.e. $\sim 9,300 \text{ yrs}$, the accretion rate for the southern protostar is $\geq 2 \cdot 10^{-4} M_{\odot} \text{ yr}^{-1}$.

IRS 9 may have an even higher accretion rate, but at near cloud velocities the HCO^+ profile is completely dominated by the pole-on outflow. At the position of IRS 9 (Fig. 3) there is a narrow self-absorption feature centered on -53 km s^{-1} , i.e. red-shifted by $\sim 4 \text{ km s}^{-1}$ from the cloud core. Inspection of spectra in the vicinity of IRS 9 show that the absorption is even broader ($\sim 4 \text{ km s}^{-1}$ wide) $5''$ to the east, corresponding to an integrated intensity of $\sim 8 \text{ K km s}^{-1} \text{ beam}^{-1}$. The velocity of the self-absorption at this position is $\sim -54 \text{ km s}^{-1}$. There is still some self-absorption $10''$ east of IRS 9, but here the self-absorption is narrower and less red-shifted. The self-absorption profiles suggest higher infall velocities for IRS 9 than for the southern protostar. The absorption profiles also show some acceleration of the infalling gas near IRS 9, but not as pronounced as towards the southern protostar.

We can also get an estimate of the accretion rate using the observed mass outflow rates using the arguments outlined by (Beuther et al. 2002). Beuther et al. assume that the outflows are jet-driven and that the momentum of the outflow is equal to that of the internal jet. They also assume that the ratio of the mass loss rate and the accretion rate is about 0.3, and are therefore able to derive mass accretion rates from the observed mass outflow rates. For IRS 9 and the southern protostar we derive mass accretion rates of $1.5 \cdot 10^{-4}$ and $7.9 \cdot 10^{-4} M_{\odot} \text{ yr}^{-1}$. If the H_2 jet also originates in the IRS 9 core, the accretion rate for IRS 9 would be considerably higher. Both methods therefore suggest that the mass accretion rate is $> 10^{-4} M_{\odot} \text{ yr}^{-1}$ and is probably closer to $10^{-3} M_{\odot} \text{ yr}^{-1}$ for IRS 9 and the southern protostar.

Such high accretion rates are more than sufficient to quench the formation of an Ultra Compact H II region (Walmsley 1995), see also Churchwell (2002), explaining why we did not detect any VLA sources in the IRS 9 region except IRS 9. Anglada (1995) found a good correlation between centimeter continuum emission (S_ν) and momentum flux (F_{out}) in low-luminosity outflow sources, with $F_{out} \propto S_\nu^{1.1}$. Although the observed relationship appears valid for the IRS 9 outflow, it would predict even higher flux densities for the H₂ jet and the protostellar outflow, both of which are non-detections at 3.6 cm. Our observation suggest that this correlation is no longer valid for young high-mass outflows.

6.3. H₂O, CH₃OH, and OH 1720 MHz masers

H₂O masers pinpoint the location of low and intermediate luminosity protostars, because the masers are excited in the protostellar disk or in dense clumps in the outflow in the immediate vicinity of the star. The IRS 9 field contains 3 H₂O masers (Table 2). The first two coincide within 1'' with IRS 9 and are most likely dense clumps of shocked gas in the high velocity outflow near IRS 9. The third H₂O maser is not associated with any known source in the IRS 9 region, nor is there any molecular outflow or shocked H₂ emission at the position of the H₂O maser. This H₂O maser is probably excited by a low-mass protostar, which is too deeply embedded to be observed in the near-IR and too compact and faint to be detectable in dust-continuum.

The class I or class Ia methanol masers like CH₃OH 7₀ → 6₁ A⁺ at 44 GHz, are thought to be associated with outflows from massive stars (Sobolev 1993). Plambeck & Menten (1990) carried out high resolution studies of the CH₃OH 8₀ → 7₁ A⁺ class Ia masers in DR 21 and DR 21(OH) and found these masers to be located along the interfaces between the outflows and cold dense ambient clouds. Johnston et al. (1992) mapped the CH₃OH 6₂ → 6₁ and 5₂ → 5₁ E transitions near 25 GHz in Orion with the VLA and found the CH₃OH masers to be located near the interface of the high-velocity outflow and the surrounding dense gas, i.e. very similar to the results of Plambeck & Menten (1990) for the DR 21 complex. Johnston et al. suggested that the methanol masers are formed behind shock fronts, and that these shock fronts are moving at right angles to the line of sight. The methanol masers in the IRS 9 region are all definitely associated with massive outflows, but the location and radial velocities of the masers suggest that they originate in the shearing layer between the outflow and the surrounding dense cloud, rather than in the bow-shocks driven by the outflow. The two masers, IRS 9-CH₃OH(1) & (2) (Table 2) are both located in the pole-on IRS 9 outflow; one in the red and one in the blue outflow lobe. The third one, IRS 9-CH₃OH(3) coincides with the H₂ jet, also seen as a very highly collimated outflow in HCO⁺ (Section 5.2). Since

their velocities are close to that of the ambient gas, it appears that they are excited in the shearing layer between the outflow and the surrounding molecular cloud. All class I methanol masers in the NGC7538 molecular cloud appear to be associated with outflows (Sandell et al, 2005, in preparation).

Most OH 1720 MHz masers are found to be coincident with H II regions, where they often coincide with OH 1665-MHz and OH 1667-MHz masers as well as with class II methanol masers (Caswell 2004). OH 1720 MHz masers, however, are also known to be associated with shock fronts from supernova remnants (Wootten 1981; Yusef-Zadeh et al. 2003), and are in rare occasions observed in shocks associated with outflows from young stars (Winnberg et al. 1981; Sandell et al. 1985). We detected a new OH 1720 MHz maser in the IRS9 field (Table 2). This OH 1720 MHz maser is located in the red-shifted outflow lobe of IRS9 and appears to be one of the rare OH 1720 MHz masers excited in the outflow of a young star. Even though both class Ia CH₃OH masers and OH 1720 MHz masers are found to be excited by outflows from young stars, they are not known to be spatially coincident, suggesting that the masing conditions must be different.

7. Conclusion

We have imaged the molecular cloud surrounding IRS9 with $\sim 5''$ angular resolution in H¹³CN J=1→0, SO 2₂ → 1₁, HCO⁺ J=1→0, and 3.4 mm continuum using the BIMA array at Hat Creek, and searched for free-free emission at 8.3 GHz with $\sim 1''$ angular resolution using the VLA. We supplemented these observations with VLA and JCMT archive data. Our main results are summarized below.

1) We find that the dense gas in the IRS9 molecular cloud is concentrated in two cold, massive cloud cores. The core centered on IRS9 has a mass of 100 - 300 M_⊙, the second core is $\sim 20''$ SE of IRS9 and has a mass of $\sim 1,000$ M_⊙. Both cloud cores harbor young stellar objects, which will most likely evolve into high-mass stars.

2) We detected IRS9 as a weak 3.6 cm source with the VLA. Comparison with 6 cm VLA archive data show a flat spectrum between 6 cm and 3.6 cm consistent with free-free emission from a collimated, ionized jet. We also detected IRS9 in dust continuum at 3.4 mm as an extended ($\sim 15''$) source centered on IRS9.

3) We resolve the previously known high velocity emission into at least three separate bipolar outflows. IRS9 drives a highly collimated extreme high-velocity outflow observed nearly pole-on. The second outflow, the H₂ jet, is equally highly collimated and jet-like and even more massive and energetic than the IRS9 outflow. This outflow is most likely powered

by an unseen object close to IRS 9. The third outflow is the most massive outflow in the IRS 9 region and has an outflow mass of $\sim 75 M_{\odot}$. The outflow has very high gas densities; the outflow is observed even in H^{13}CN . The center of symmetry for this outflow coincides with a strong, relatively compact H^{13}CN peak in the southern core with a mass $\geq 250 M_{\odot}$, which appears to host a very young massive protostar.

4) Both IRS 9 and the southern protostar show red-shifted self-absorption profiles in HCO^+ , consistent with high mass accretion. The inferred mass accretion rates for both IRS 9 and the southern protostar are a few times 10^{-4} to $\sim 10^{-3} M_{\odot} \text{ yr}^{-1}$. Such high accretion rates are sufficient to quench the formation of an H II region.

5) Both IRS 9 and the southern protostar drive hot outflows. Examination of previously published data and single dish H_2CO spectra suggest gas temperatures of 180 K for the IRS 9 outflow and ≥ 80 K for the protostellar outflow.

6) We believe that the HCO^+ emission is enhanced by at least a factor of 30 in the hot IRS 9 outflow. The HCO^+ abundance may be normal in the other two outflows.

7) The three class I methanol masers discovered in the IRS 9 region all coincide with massive, high velocity outflows. Since the methanol masers have radial velocities close to the cloud velocity, it seems that they are most likely excited in the shearing layer between the high velocity gas and the ambient cloud. We also report the detection of an OH 1720 MHz OH maser in the IRS 9 outflow, which is excited in conditions similar to that of the methanol masers. The OH maser is not spatially coincident with any of the methanol masers.

G. S. would like to thank Ed Churchwell for useful and stimulating discussions. The BIMA array is operated by the Universities of California (Berkeley), Illinois, and Maryland with support from the National Science Foundation. This work was supported in part by NSF Grant AST 0228963 to the University of California.

REFERENCES

- Anglada, G. 1995, *Rev. Mex. Astron. Astrofis. Ser. de Conf.*, 1, 67
- Beetz, M., Elsässer, H., Poulakos, C., & Weinberger, R. 1976, *A&A*, 50, 41
- Beltrán, M. T., Gueth, F., Guilloteau, S., & Dutrey, A. 2004, *A&A*, 416,631
- Beuther, H., & Schilke, P. 2004, *Science*, 303, 1167

- Beuther, H., Hunter, T. R., Zhang, Q., Sridharan, T. K., Zhao, J. -H., Sollins, P., Ho, P. T. P., Ohashi, N., Su, J., Lim, J., & Liu, S. -Y. 2004, ApJ, in press
- Beuther, H., Schilke, P., & Gueth, F. 2004, ApJ, 608, 330
- Beuther, H., Schilke, P., & Stanke, T. 2003, A&A, 408, 601
- Beuther, H., Schilke, P., Sridharan, T. K., Menten, K. M., Walmsley, C. M., & Wyrowski, F. 2002a, A&A, 383, 892
- Beuther, H., Schilke, P., Gueth, F., McCaughrean, M., Andersen, M., Sridharan, T. K., & Menten, K. M. 2002b, A&A, 387, 931
- Blake, G. A., Sutton, E. C., Masson, C. R., & Phillips, T. G. 1987, ApJ, 315, 621
- Bohlin, R. C., Savage, B. D., & Drake, J. F. 1978, ApJ, 224, 132
- Bontemps, S., André, P., Terebey, S., & Cabrit, S. 1996, A&A, 311, 858
- Cabrit, S., & Bertout, C. 1992, A&A, 261, 274
- Campbell, B., & Persson, S. E. 1988, AJ, 95, 1185
- Caswell, J. L. 2004, MNRAS, 349, 99
- Cesaroni, R., Felli, M., Testi, L., Walmsley, C. M., & Olmi, L. 1997, A&A, 325, 725
- Chernin, L. M., Masson, C., & Fuller, G. A. 1994, ApJ, 436, 741
- Chini, R., Hoffmeister, V., Kimeswenger, S., Nielbrock, M., Nürnberger, D. Schmidtobreck, L., & Sterzik, M. 2004, Nature, 429, 155
- Churchwell, E. 2002, ARA&A, 40, 27
- Crampton, D., Georgelin, Y. M., & Georgelin, Y. P. 1978 A&A, 66, 1
- Davis, C.J., Moriarty-Schieven, G., Eislöffel, J., Hoare, M. G., & Ray, T.P. 1998, AJ, 115, 1118
- Eiroa, C., Lenzen, R., & Gomez, A. I. 1988, A&A, 190, 283
- Garden, R. P., & Carlstrom, J. E. 1992, ApJ, 392, 602
- Gibb, A. G., Hoare, M. G., Little, L. T., & Wright, M. C. H. 2003, MNRAS, 339, 1011
- Hasegawa, T., & Mitchell, G. F. 1995, ApJ, 441, 665

- Henning, Th., Schreyer, K., Launhardt, R., & Burkert, A. 2000, *A&A*, 353, 211
- Hildebrand, R. H. 1983, *QJRAS*, 24,267
- Hillenbrand, L. A. 1977, *AJ*, 113, 1733
- Johnston, K. J., Gaume, R., Stolovy, S., Wilson, T. L., Walmsley, C. M., & Menten, K. M. 1992, *ApJ*, 385, 232
- Kameya, O., Hasegawa, T. I., Hirano, M., Takakubo, K. & Seki, M. 1989, *ApJ*, 339, 222
- Kameya, O., Morita, K. -I., T.I., Kawabe, R., & Ishiguro, M. 1989, *ApJ*, 355, 562
- Keto, E. R., Ho, P. T. P., & Haschick, A. D. 1988, *ApJ*, 324, 920
- Leung, C. M., & Brown, R. L. 1977, *ApJ*, 214, L73
- Maeder, A., & Behrend, R. 2002, *Ap&SS*, 281, 75
- Mangum, J., & Wootten, A. 1993, *ApJS*, 89, 123
- McKee, C. F., & Tan, J. C. 2002, *Nature*, 416, 59
- Mitchell, G. F. 1984, *ApJ*, 287, 665
- Mitchell, G. F., Maillard, J.-P., Allen, M., Beer, R., & Belcourt, K. 1990, *ApJ*, 363, 554
- Mitchell, G. F., & Hasegawa, T. 1991, *ApJ*, 371, L33
- Moreno, M. A., & Chavarría-K, C. 1986, *A&A*, 161, 130
- Plambeck, R. L., Wright, M. C. H., Welch, J. H., Bieging, J. H., Baud, B., Ho, P. T. P., & Vogel, S. N. 1982, *ApJ*, 259, 617
- Plambeck, R. L., & Menten, K. M. 1990, *ApJ*, 364, 555
- Reynolds, S. P. 1986, *ApJ*, 304, 713
- Sandell, G., & Sievers, A. 2004, *ApJ*, 600, 269
- Sandell, G., Wright, M., & Forster, J. R. 2003, *ApJ*, 590, L45
- Sandell, G., Nyman, L. A., Haschick, A., & Winnberg, A. 1985, in *Lecture Notes in Physics* 237, *Nearby Molecular Clouds*, Ed. G. Serra (Springer-Verlag: Berlin), p. 234

- Sault, R. J., Teuben, P. J., & Wright, M. C. H., 1995, in ASP Conf. Ser. 77: Astronomical Data Analysis Software and Systems IV, Eds. R.A. Shaw, H.E. Payne, and J.J.E. Hayes (Astronomical Society of the Pacific: San Francisco), p. 433
- Schwartz, A., & Pratap, P. 2002, BAAS, 34, 1136
- Shah, R. Y., & Wootten, A. 2001, ApJ, 554, 933
- Shepherd, D. S., & Churchwell, E. 1996, ApJ, 472, 225
- Shirley, Y. L., Evans II, N. J., Rawlings, J. M. C., & Gregersen, E. M. ApJS, 131, 249
- Sobolev, A. M. 1993, Astron. Lett, 19, 293
- Swade, D. A. 1989, ApJ, 345, 828
- Tamura, M., Gatley, I., Joyce, R. R., Ueno, M., Suto, H., & Sekiguchi, M. 1991, ApJ, 378, 611
- Tielens, A. G. G. M., Tokunaga, A. T., Geballe, T. R., & Baas, F. 1991, ApJ, 381, 181
- van der Tak, F. F. S., van Dishoeck, E. F., Evans II, N. J., & Blake, G. A. 2000, ApJ, 537
- Walmsley, M. C. 1995, Rev. Mex. Astron. Astrofis. Ser. de Conf., 1, 137
- Welch, W. J., Dreher, J. W., Jackson, J. M., Terebey, S., & Vogel, S. N. 1987, Science, 238, 1550
- Werner, M. W., Becklin, E. E., Gatley, I., Matthews, K., Neugebauer, G., & Wynn-Williams, C. G. 1979, MNRAS, 188, 463
- Wilson, T. L., & Rood, R. T. 1994, ARA&A, 32, 192
- Winnberg, A., Graham, D., Walmsley, C. M., & Booth, R. S. 1981, A&A, 93, 79
- Wootten, A. 1981, ApJ, 245, 105
- Yusef-Zadeh, F., Wardle, M., Rho, J., & Sakano, M. 2003, ApJ, 319
- Zhang, Q., Hunter, T. R., Brand, J., Sridharan, T. K., Molinari, S., Kramer, M. A., & Cesaroni, R. 2001, ApJ, 552, L167
- Zhang, Q., Ho, P. T. P., & Ohashi, N. 1998, ApJ, 494, 636
- Zhang, Q., Hunter, T. R., & Sridharan, T. K. 1998, ApJ, 505, L151

Zhang, Q., & Ho, P. T. P. 1997, ApJ, 488, 241

Zheng, X. -W., Zhang, Q, Ho, P. T. P., & Pratap, P. 2002, ApJ, 550, 301

Zhou, S., Evans II, N. J., Kömpe, C., & Walmsley, C. M. 1993, ApJ, 404, 232

Zhou, S. 1992, ApJ, 394, 204

Table 1. Continuum positions and flux densities for IRS 9

Frequency [GHz]	$\alpha(2000.0)$ [h m s]	$\delta(2000.0)$ [$^{\circ}$ ' '']	$\theta_a \times \theta_b^a$ ['' \times '']	P.A. [$^{\circ}$]	S_{peak} [mJy]	S_{int} [mJy]	ref
4.86	23 14 01.72 \pm 0.04	+ 61 27 19.5 \pm 0.3	2.4 \pm 1.2 \times 1.1 \pm 1.1	...	0.32 \pm 0.11	1.00 \pm 0.44	1
8.46	23 14 01.77 \pm 0.006	+ 61 27 19.8 \pm 0.06	0.7 \pm 0.5 \times 0.1 \pm 0.1	+105 \pm 60	0.44 \pm 0.06	0.76 \pm 0.15	1
89 ^b	23 14 01.63 \pm 0.05	+ 61 27 20.1 \pm 0.3	21 \pm 3 \times 10 \pm 1	+74 \pm 1	18 \pm 3	85 \pm 10	1
107	23 14 01.78 \pm 0.07	+ 61 27 20.2 \pm 0.3	point-source	43	2
110	point-source	95	2
2.2 μm^c	23 14 01.62 \pm 0.14	+ 61 27 20.3 \pm 1.0	313.5	3

^aDeconvolved source size FWHM

^bThe BIMA continuum image can also be fit with a two component Gaussian fit, in which case we find a unresolved point-source at the center with a flux density of 8 ± 4 mJy.

^cUsing the 2.12 μm image of Davis et al. (1998) and IRS 10 (Campbell & Persson 1988) as an astrometric reference gives: $23^h 14^m 01^s.76 \pm 0^s.07$, $+ 61^{\circ} 27' 20''.5 \pm 0''.5$.

References. — (1) This work; (2) van der Tak et al. (2000); (3) Tamura et al. (1991)

Table 2. Masers in the IRS 9 field

Name	$\alpha(2000.0)$ [h m s]	$\delta(2000.0)$ [$^{\circ}$ ' "]	V_{lsr} km s $^{-1}$	Flux [Jy]	ref
H ₂ O					
IRS 9-H ₂ O(1)	23 14 01.75	+61 27 19.7	−61.9	1.7	1
IRS 9-H ₂ O(2)	23 14 01.72	+61 27 19.9	−74.3	3.1	1
IRS 9-H ₂ O(3)	23 13 58.60	+61 27 04.5	−68.8	16.1	2
OH 1720-MHz					
IRS 9-OH	23 14 03.15	+61 27 21.4	−54.7	1.4	2
CH ₃ OH 7 ₀ → 6 ₁ A ⁺					
IRS 9-CH ₃ OH(1)	23 14 01.99	+61 27 21.8	−57.7	2.4	2
IRS 9-CH ₃ OH(2)	23 14 00.82	+61 27 19.4	−56.3	1.5	2
IRS 9-CH ₃ OH(3)	23 14 03.02	+61 26 46.7	−57.0	0.70	2

References. — (1) Kameya et al. (1990); (2) This work

Table 3. Outflow parameters corrected for opacity and inclination.

Outflow	t_{dyn}	M_{blue}	M_{red}	M_{out}	P_{out}	F_{out}	E_{kin}	L_{mec}
IRS 9 ^a	9,500	8	8	16	215	21	4	10 ^b
H ₂ -jet	19,500	21	10	31	620	30	14	29
Protostar	9,300	34	15	59	1,100	116	30	200

Note. — Outflow masses are computed from HCO⁺ for blue-shifted emission and from CO for red-shifted emission (except for IRS 9, where all parameters are derived from HCO⁺). Masses, M_{blue} , M_{red} , and total mass, M_{out} , are given in [M_{\odot}]. momentum P , in [$M_{\odot} \text{ km s}^{-1}$], momentum flux F_{out} , in [$10^{-3} M_{\odot} \text{ km s}^{-1} \text{ yr}^{-1}$], kinetic energy E_{kin} , in [10^{46} ergs], and mechanical luminosity, L_{mec} , in [L_{\odot}].

^aSince we used too small a bandwidth to cover the whole velocity range in HCO⁺, we have estimated the dynamical time scale from the observed maximum CO velocity, 77 km s⁻¹ and not from HCO⁺. Outflow masses are based on HCO⁺.

^bThe luminosity from extreme high velocity CO emission not seen in HCO⁺, would add 10 L_{\odot} to the luminosity from the red-shifted outflow alone.

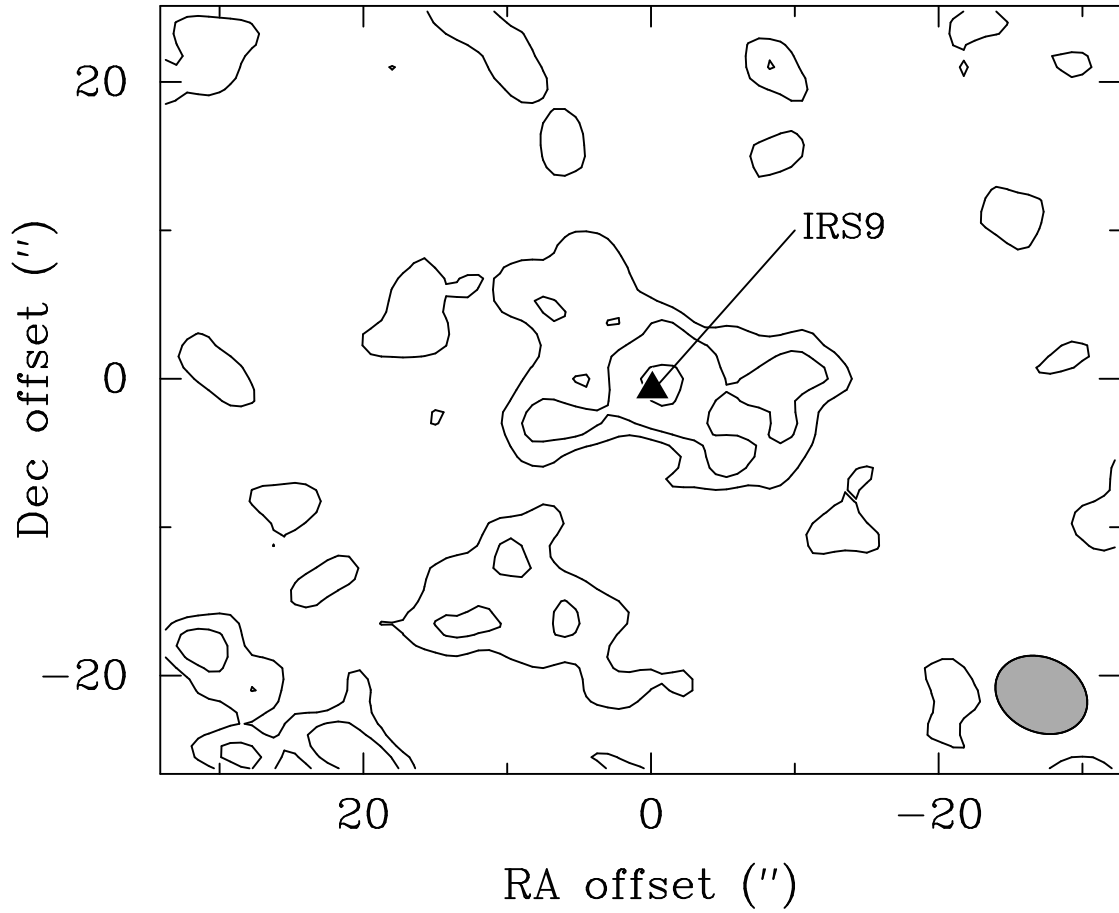


Fig. 1.— Continuum emission from IRS9 at 89 GHz observed with BIMA. The lowest contour is at 4 mJy beam^{-1} with steps of 4 mJy beam^{-1} . The position of the marginally extended (size $\leq 1''$) VLA source at 8.3 GHz is plotted with a filled triangle and labeled as IRS9. The beam FWHM of BIMA is plotted in the bottom right corner of the image.

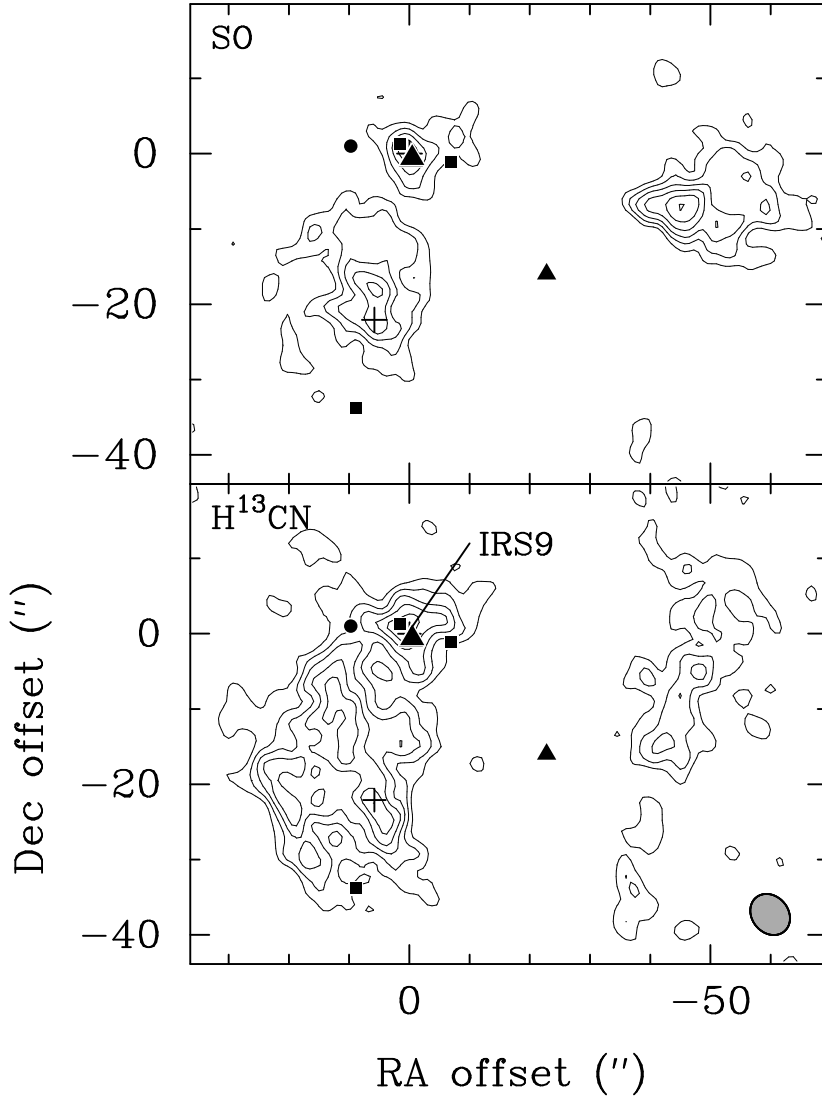


Fig. 2.— BIMA contour images of integrated H^{13}CN and SO emission. The offsets are relative to the field center, $\alpha_{2000.0} = 23^{\text{h}} 14^{\text{m}} 01.^{\text{s}}778$, $\delta_{2000.0} = +61^{\circ} 27' 20''.5$). H^{13}CN is integrated over the velocity interval -45 to -70 km s^{-1} , which also includes some high velocity gas (see text). SO is integrated over a narrower velocity interval, -53 to -61 km s^{-1} , to exclude high-velocity emission. The peak flux of H^{13}CN and SO is 0.0854 and 0.135 $\text{Jy km s}^{-1} \text{beam}^{-1}$, respectively. The contour levels start at 0.03 and 0.04 $\text{Jy km s}^{-1} \text{beam}^{-1}$ for H^{13}CN and SO , respectively. For both molecules we plotted eight contours between the lowest level and the peak position. The filled triangles mark known H_2O masers, the filled squares are methanol class I masers, the cross marks the position of the southern protostar, and the filled circle is the $\text{OH } 1720$ MHz maser (see Table 2). The beam FWHM is shown in the bottom right corner of the lower panel.

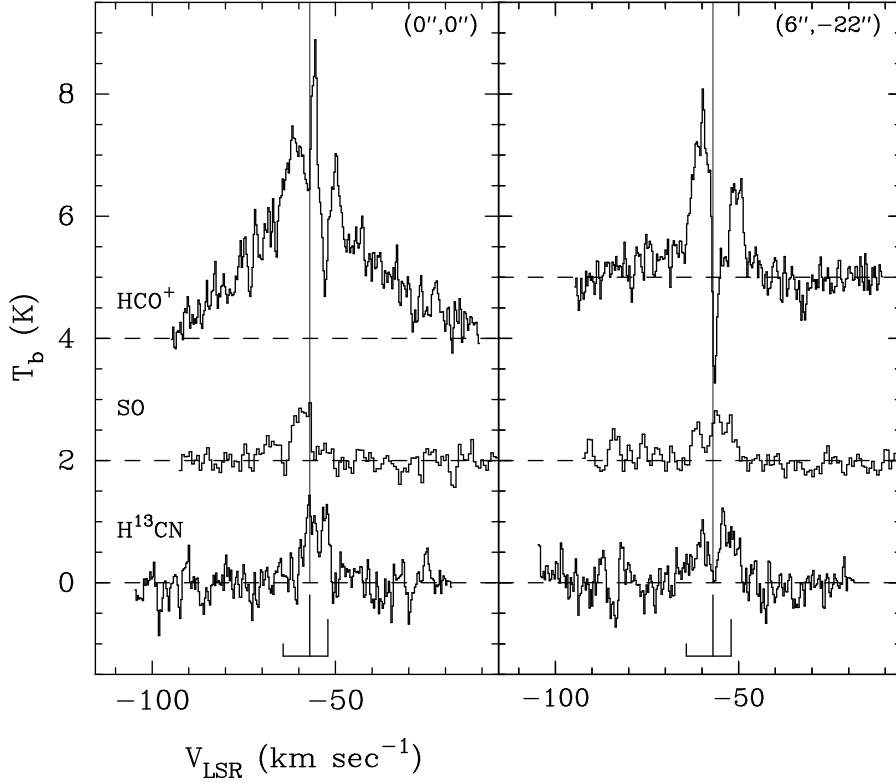


Fig. 3.— High resolution BIMA spectra of H^{13}CN , SO , and HCO^+ towards IRS 9, $(0'', 0'')$, and the southern protostar at $(6'' -22'')$. IRS 9 and the southern protostar show deep redshifted self-absorption in HCO^+ and evidence for high velocity emission in H^{13}CN and SO . The protostar also shows deep self-absorption in the $F = 2 \rightarrow 1$ transition of H^{13}CN . The position and relative intensity of the H^{13}CN hyperfine components are indicated in the line drawings below the H^{13}CN spectra.

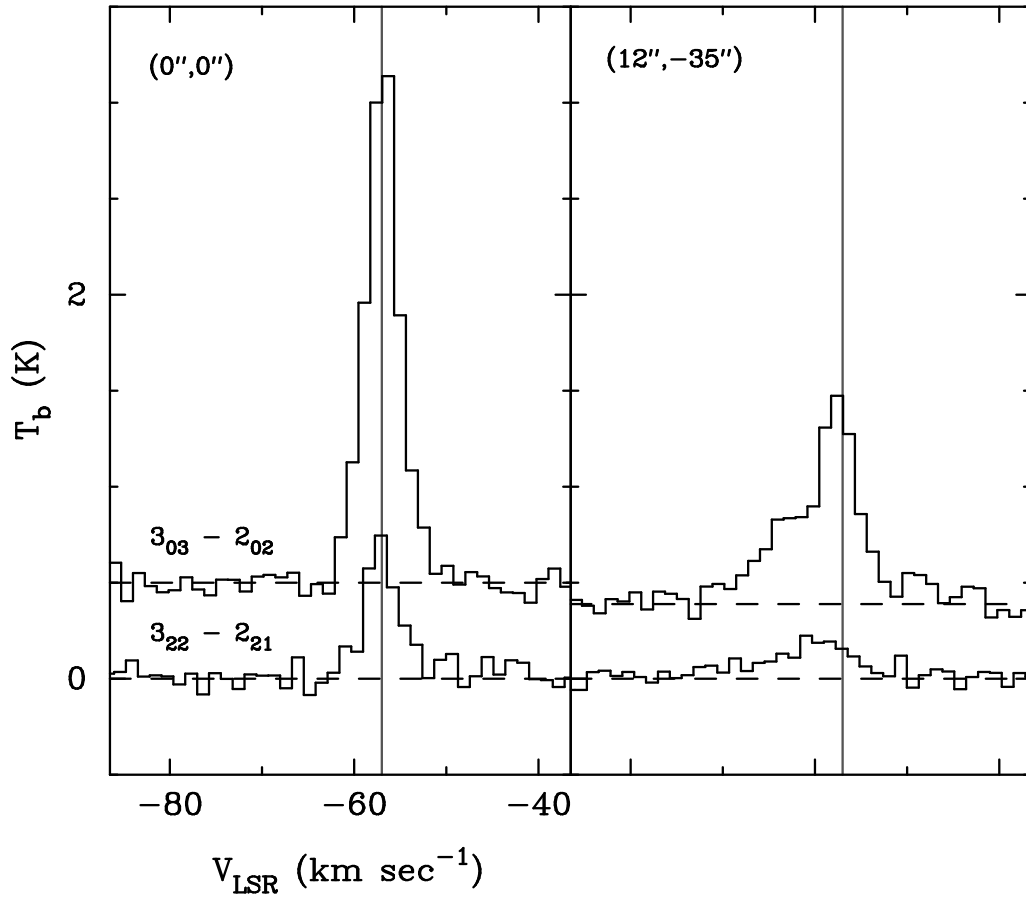


Fig. 4.— Single dish JCMT spectra of the 1.4 mm $3_{2,2} - 2_{2,1}$ and $3_{0,3} - 2_{0,2}$ transitions of H_2CO towards IRS9 and a position near the southern protostar ($12'', -35''$); the latter position shows strong blue-shifted high velocity gas in both transitions. The spectra have been binned to a resolution of 1.4 km s^{-1} .

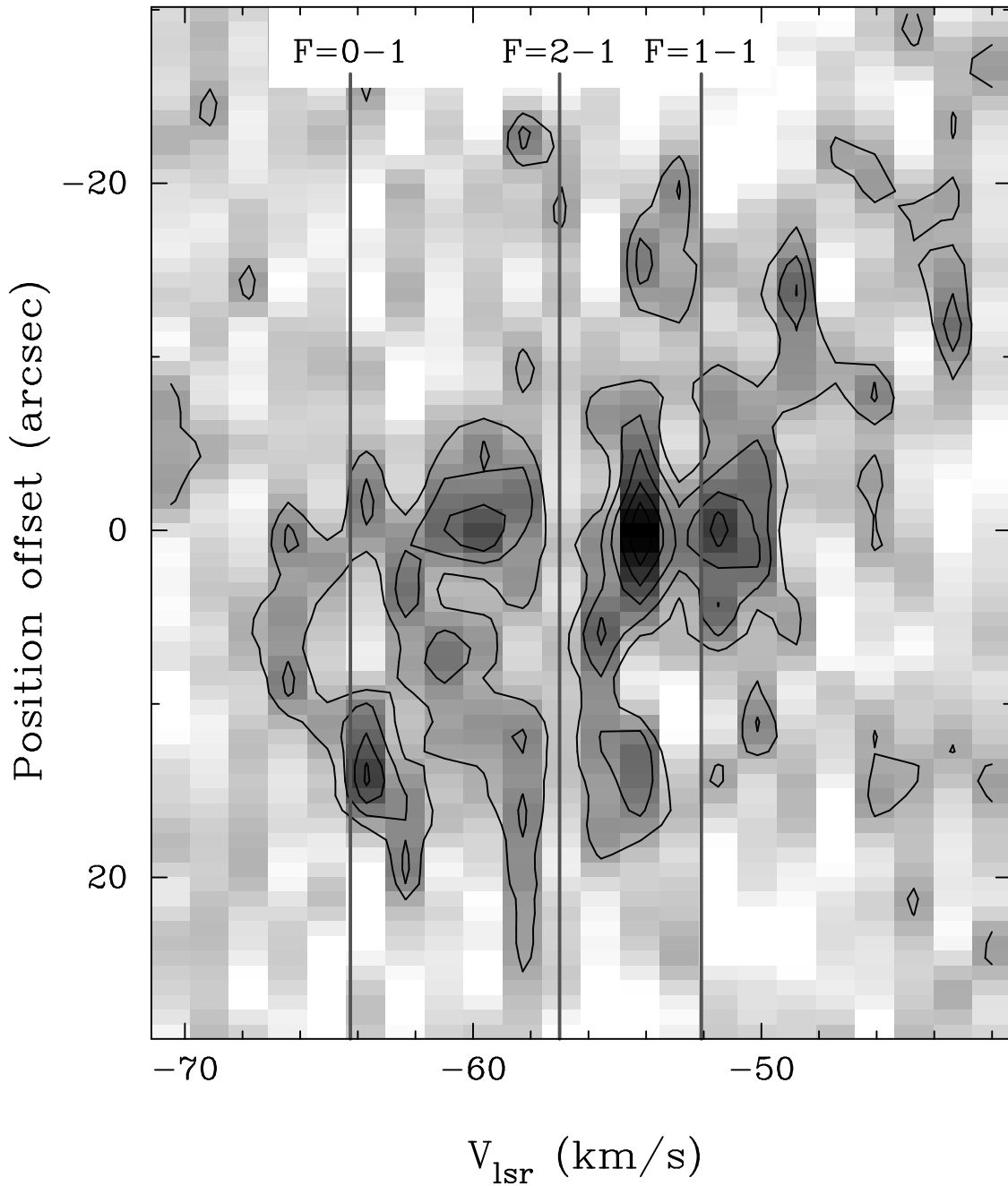


Fig. 5.— BIMA position velocity plot of H¹³CN (binned to $\Delta V = 1.4 \text{ km s}^{-1}$) through the protostellar core at a p.a. of 118° , i.e. approximately orthogonal to the outflow powered by a protostar embedded in this dense core. The main hyperfine component, $F=2 \rightarrow 1$ is completely absorbed at the systemic velocity of the cloud core, -57 km s^{-1} . The velocity of the three hyperfine components relative to the systemic cloud velocity is indicated by gray vertical lines. Positive offsets are to the south.

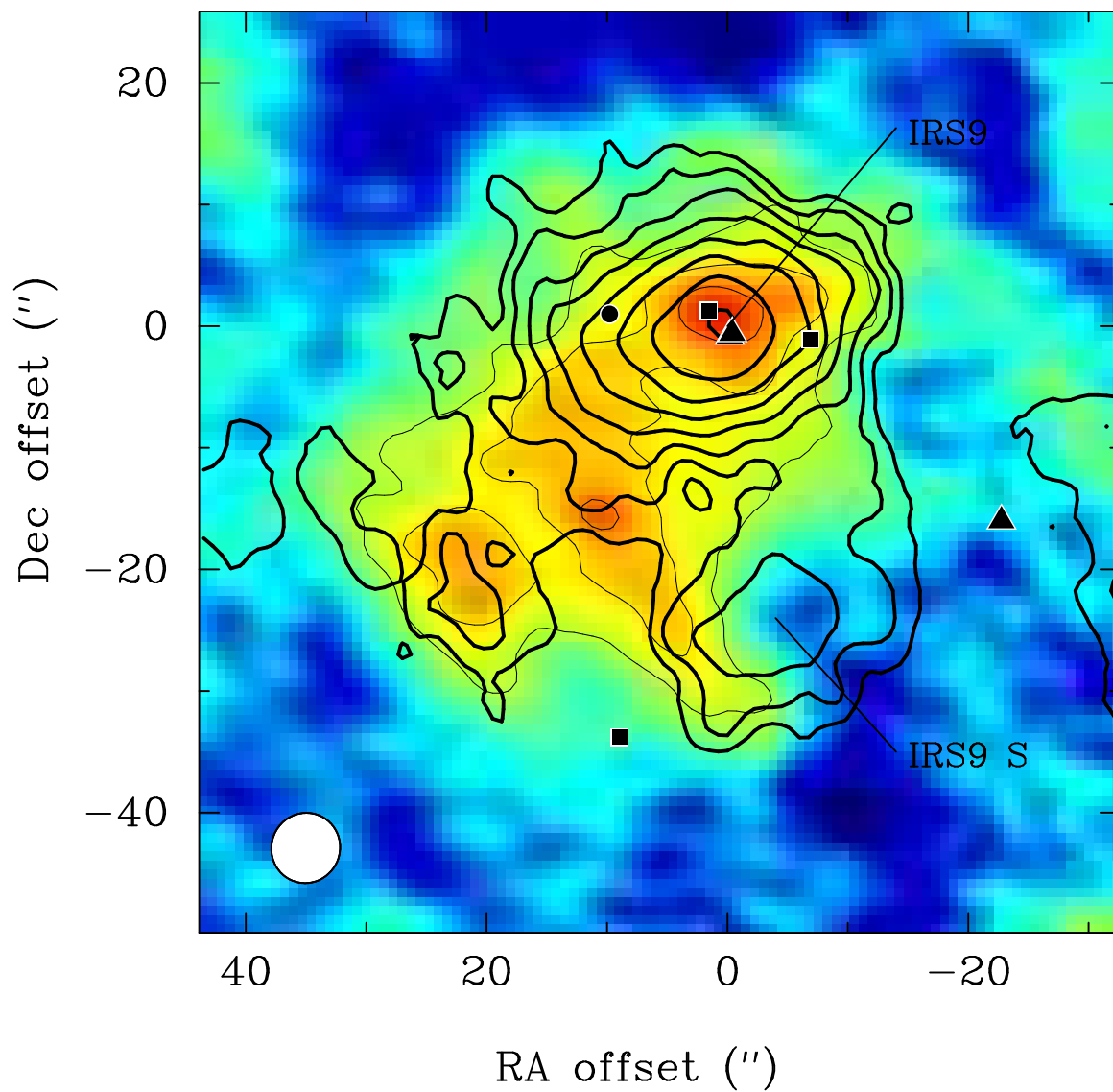


Fig. 6.— Contour plot (thick contours) of the 450 μm SCUBA emission smoothed to $10''$ -resolution and overlaid on a pseudo color image of the integrated H^{13}CN emission. The position of the masers are plotted as in Fig. 2. The latter is enhanced with thin contours better to show the extent of the H^{13}CN emission. The FWHM of the BIMA beam is shown in the bottom left corner of the image.

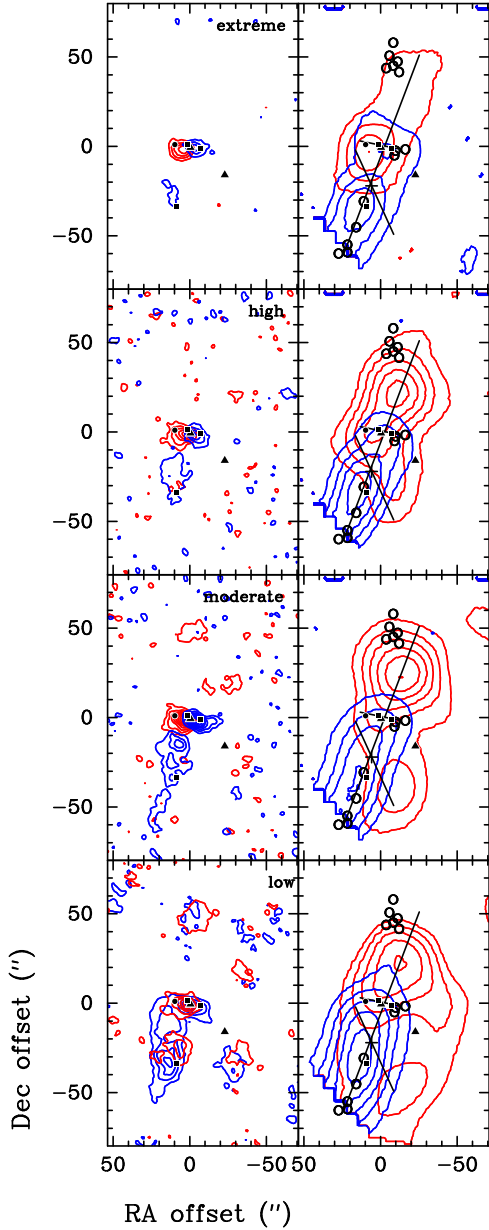


Fig. 7.— The left panels shows contours of the high velocity emission of HCO⁺ divided into four velocity intervals: low, intermediate, high, and extreme, see Section 5 for details. The velocity intervals are labeled at the top of each sub-panel. The right panels show the high velocity CO emission over the same velocity range. The BIMA HCO⁺ images have an angular resolution of $\sim 6''$, while the JCMT CO images have a resolution of $\sim 22''$. The position of the masers are plotted as in Fig. 2. In the right hand panel the solid lines mark the symmetry axis of the three outflows as determined from HCO⁺. We have additionally marked all shocked H₂ knots visible in the narrowband H₂ image from Davis et al. (1998).

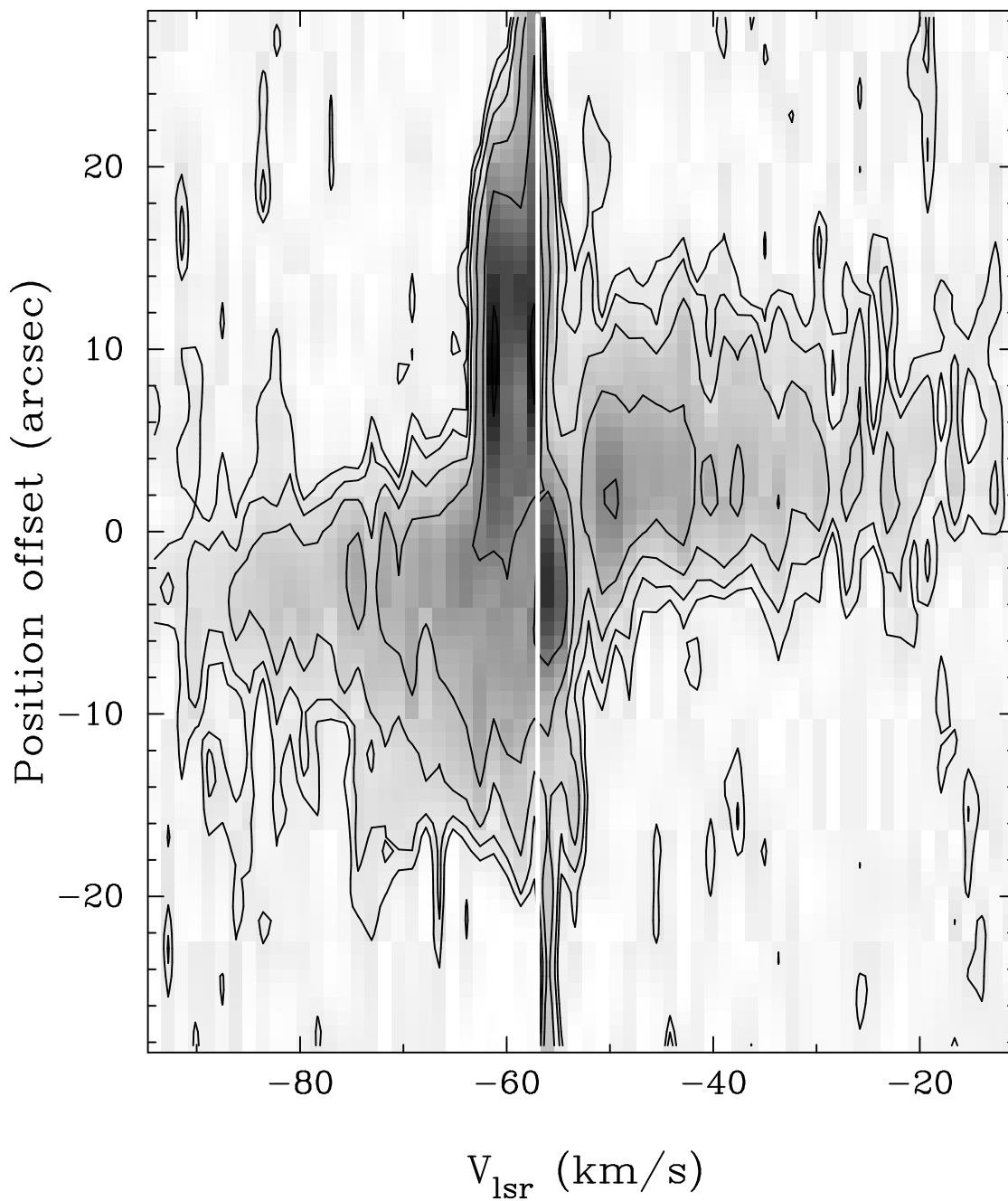


Fig. 8.— BIMA position velocity plot of HCO⁺ through IRS9 at a p.a. of 80°. The systemic velocity of -57 km s^{-1} is indicated by the white vertical line. Red-shifted self-absorption is observed over the whole outflow. To the east another cloud component at $\sim -63 \text{ km s}^{-1}$ is detected. Positive offsets are to the east.

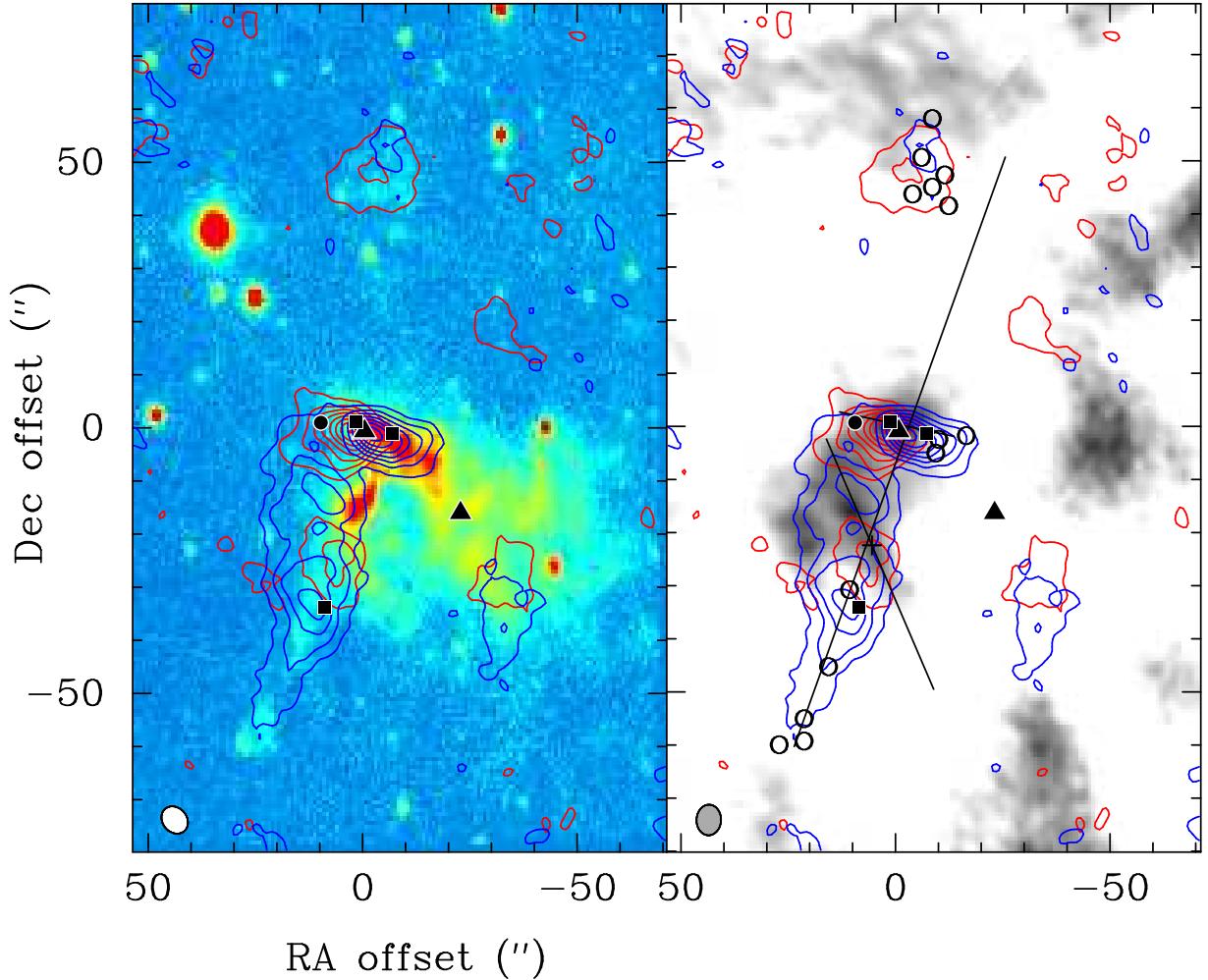


Fig. 9.— The left panel shows contour maps of HCO^+ integrated over low and intermediate red and blue-shifted velocities (see text) overlaid on the narrowband $2.12 \mu\text{m}$ H_2 image in color. The blue-shifted HCO^+ emission follows the H_2 jet. About $50''$ north of IRS9 we observe faint red- and some blue-shifted emission coinciding with a cluster of shocked H_2 knots. Another region of faint red- and blue-shifted high velocity gas is observed $\sim 50''$ SW of IRS9 in the southern part of the reflection nebula. The right panel shows the same HCO^+ high velocity contours overlaid on the gray scale image of integrated H^{13}CN emission. The compact red-shifted outflow lobe $\sim 25''$ south of IRS9 coincides with the H^{13}CN peak. The position of the masers are plotted as in Fig. 2 and in the right hand panel the open squares show the location of all shocked H_2 knots. The FWHM of the BIMA beam is shown in the bottom left corner, left panel: HCO^+ , right panel: H^{13}CN .

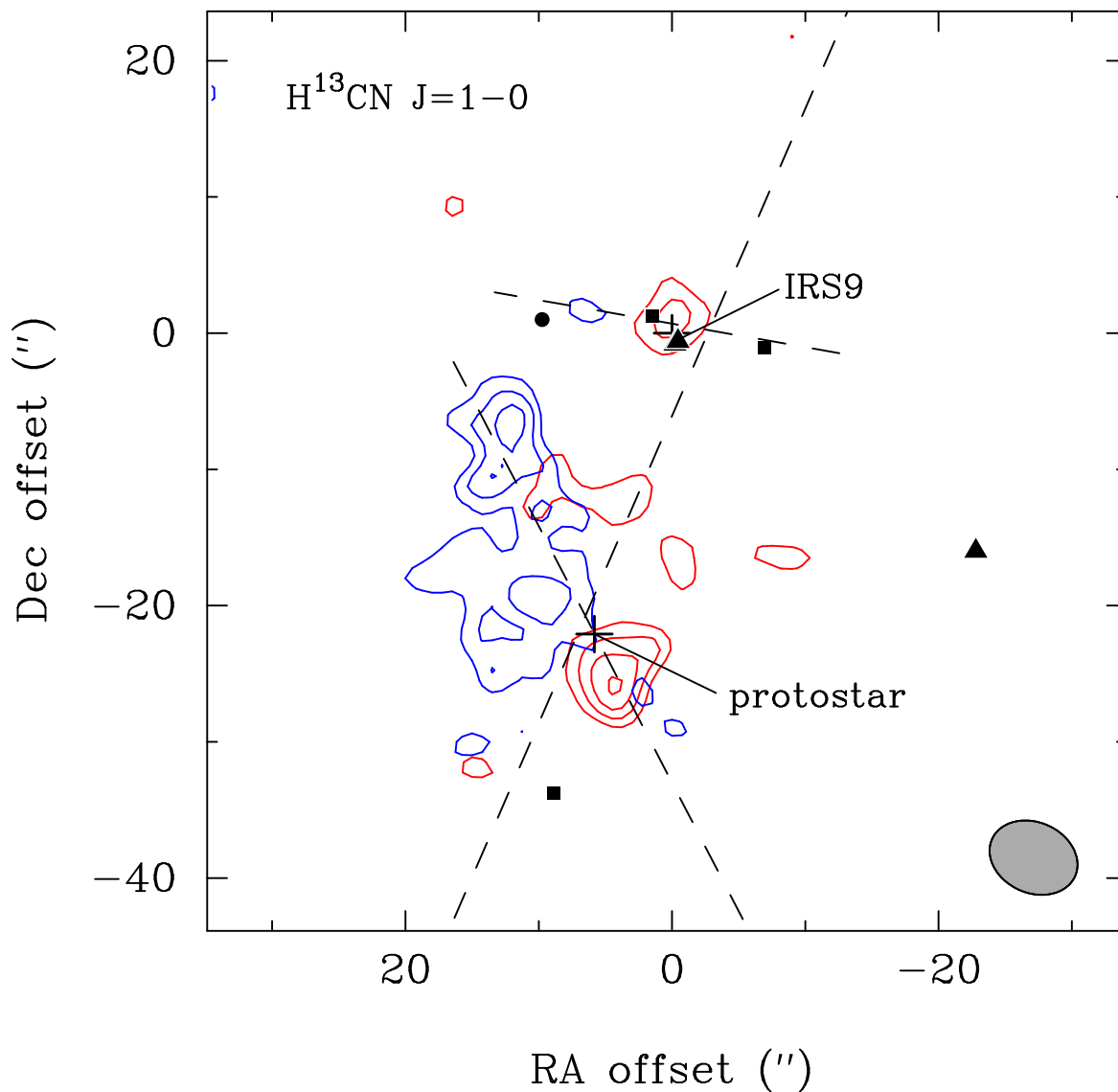


Fig. 10.— Contour image of red- and blue-shifted high velocity emission in $\text{H}^{13}\text{CN } J=1\rightarrow 0$. The red-shifted emission is integrated over 10 km s^{-1} from -53.5 km s^{-1} , while the blue-shifted emission is integrated from -63 km s^{-1} to -69.7 km s^{-1} , but excluding a 4 km s^{-1} window around the faint $F = 1 - 1$ hyperfine component. The symmetry axis and extent of the three high velocity HCO^+ outflows discussed in the text are drawn by dotted lines. The position of the masers are plotted as in Fig. 2. The protostellar source lies between the red- and the blue-shifted outflow lobe of H^{13}CN . Faint red-shifted emission is observed towards IRS9. The FWHM of the BIMA beam is shown in the bottom right corner.